Photo-gyrotactic bioconvection

C. R. WILLIAMS† AND M. A. BEES

Department of Mathematics, University of Glasgow, University Gardens, Glasgow G12 8QW, UK

Many microorganisms exhibit taxes, biased swimming motion relative to a directional stimulus. Aggregations of cells with densities dissimilar to the medium in which they swim can induce hydrodynamic instabilities and bioconvection patterns. Here, three novel and mechanistically distinct models of the interaction of the two dominant taxes in suspensions of swimming phototrophic algae are presented: phototaxis, swimming towards or away from light, and gyrotaxis, a balance between viscous and gravitational torques. The descriptions are accordant with, and extend, recent rational models of bioconvection. In particular, the first model is for photokinesis–gyrotaxis, the second varies the cells' centre-of-mass offset, and the third introduces a reactive phototactic torque associated with the propulsive flagellar apparatus. Equilibria and linear-stability analysis in a layer of finite depth are analysed in detail using analytical and numerical methods. Results indicate that the first two models, despite their different roots, remarkably are in agreement. Penetrative and oscillatory modes are found and explained. Dramatically different behaviour is obtained for the model with phototactic torques: instabilities arise even in the absence of fluid motion due to induced gradients of light intensity. Typically, the response of microorganisms to light is multifaceted and thus some combination of the three models is appropriate. Encouragingly, qualitative agreement is found with recent experimental measurements on the effects of illumination on dominant pattern wavelength in bioconvection experiments. The theory may be of some interest in the emergent field of bioreactor design.

Key words: bioconvection, instability, swimming/flying

1. Introduction

The term 'bioconvection' was coined by Platt in 1961 to describe the phenomenon of pattern formation in shallow suspensions of motile microorganisms that are more dense than the fluid in which they swim (Platt 1961). Patterns are initiated by swimming cells whose intrinsically random orientations are biased by certain stimuli; a response that, in essence, guides cells towards more favourable locations. These responses are termed taxes. Examples include phototaxis, movement towards or away from light, gravitaxis, a bias in direction due to gravity, and gyrotaxis, a balance between a gravitational torque (typically the cells are bottom heavy) and viscous torques. In this study, all three taxes are coalesced into one model.

In suspensions of upswimming cells, bioconvection patterns may occur via a Rayleigh–Taylor-type of instability at the surface of the fluid from where a sublayer of cells that is denser than the medium overturns. Furthermore, gyrotaxis can cause

† Email address for correspondence: chll1@bas.ac.uk

an instability even in the absence of a fluid boundary since gyrotactic cells swim towards regions of marginally downwelling fluid (Kessler 1985). The added mass of the cells amplifies the downwelling so that the fluid sinks faster. Illumination of the suspension has a significant effect on the bioconvection patterns that form (see Wager 1911; Kessler 1985, 1986). Cells tend to swim towards the light source when light intensity I is below a critical value I_c (positive phototaxis) and away from the light source when $I > I_c$ (negative phototaxis). Thus, if possible, cells attempt to converge on a location at which $I = I_c$. Self-shading, where cells absorb and scatter light, creates a non-uniform distribution of light intensity throughout the suspension layer and determines locations at which $I = I_c$. With illumination from above, it is conceivable that a steady concentrated sublayer could form such that cells above the sublayer swim down and those below swim up. Only the lower region would be gravitationally unstable, providing an opportunity for penetrative bioconvection: flows from the unstable region thrust into the stable region and result in motions that utilize the whole fluid layer (Veronis 1963; Straughan 1993). However, bioconvective instabilities (particularly due to gyrotaxis) are likely to occur before steady sublayers are realized.

Many different models of bioconvection have been proposed over the last few decades. Plesset & Winet (1974) modelled bioconvection as a Rayleigh–Taylor instability; the most unstable wavelength (the one that grows most rapidly from steady state) was computed as a function of the cell concentration and depth of the stratified system. The first self-consistent hydrodynamic theory for the onset of bioconvection was presented by Childress, Levandowsky & Spiegel (1975). The model incorporated purely upward-swimming cells, caused by an off-centre mass distribution, in a suspension of finite depth. A Boussinesq approximation was used, such that the only way in which the cells affect the fluid flow is through vertical variations in the suspension density. The first models to include gyrotaxis as well as gravitaxis in bioconvection problems were presented by Pedley, Hill & Kessler (1988) for an infinite suspension and by Hill *et al.* (1989) for a suspension of finite depth. Both models were based on the upswimming-only models of Childress *et al.* (1975), but the cell-swimming direction was calculated in a deterministic fashion as a function of vorticity and the rate-of-strain tensor using the gyrotactic theory of Pedley & Kessler (1987).

However, Pedley & Kessler (1990) remonstrated that using a strongly random isotropic diffusion tensor that is independent of gyrotaxis is inconsistent with modelling swimming velocity as deterministic, as in Pedley *et al.* (1988) and Hill *et al.* (1989). Hence, they proposed modelling the cell-swimming direction in a probabilistic fashion, using techniques similar to those for colloidal particles subjected to Brownian motion (as in, for example, Hinch & Leal 1972; Leal & Hinch 1972). They employed this formulation to calculate the mean cell-swimming direction and cell diffusion tensor, and investigated pattern formation in a suspension of infinite depth. Bees & Hill (1998) further exploited this approach to conduct a linear-stability analysis for a suspension of finite depth. Here, we shall extend the model of Pedley & Kessler (1990), amalgamating phototactic descriptions, for a suspension of finite depth, whilst utilizing analysis from Bees & Hill (1998).

The models described above do not include the effects of illumination or thus phototaxis. The first attempt at modelling purely phototactic bioconvection (i.e. no orientation bias due to gravity) was presented by Vincent & Hill (1996) for a suspension of microorganisms in a shallow layer of infinite horizontal extent illuminated from above. Following the approach of Childress *et al.* (1975), they
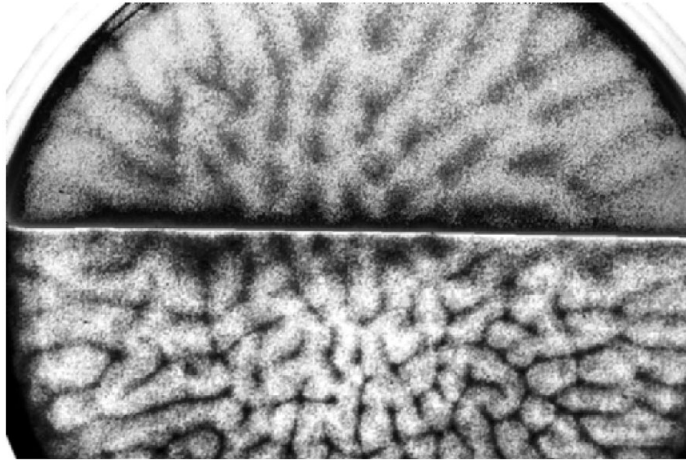
FIGURE 1. Descending bioconvection plumes (dark regions) in a Petri dish (5 cm diameter, suspension is 0.4 cm deep, 10^6 cells cm^{-3}). The illumination is white (2710 lux) from below and is half covered by a red filter (bottom of the picture, 660 nm, contrast enhanced). In the lower half, the cells do not respond to the red illumination and a web of fine gyrotactically focused structures emerges, initiated by an overturning instability due to gravitaxis. In the upper half, the bright white light biases some cells to swim upwards (negative phototaxis), supporting the emergence of an overturning instability but suppressing gyrotaxis, resulting in broader plumes (see Williams & Bees 2011).

implemented a simple up–down phototactic response as a function of light intensity at each cell, and diffusion was modelled as a constant orthotropic tensor. They assumed that the only effect the cells have on the suspension is due to their negative buoyancy; other contributions to the bulk stress were neglected. Vincent & Hill (1996) modelled light intensity with the well-known Beer–Lambert law for weak scattering, as suggested by Kessler (1989). Ghorai & Hill (2005) used this model in a two-dimensional layer confined between a rigid bottom and a stress-free top to numerically investigate phototactic bioconvection. They also corrected a significant error in the equilibrium solution of Vincent & Hill (1996). Recently, Ghorai, Panda & Hill (2010) have explored the effects of light scattering, finding unusual bimodal steady-state profiles in some parameter regimes.

Figure 1 illustrates the important effect that light has on bioconvection patterns. As yet, no model combining phototaxis with gravitaxis and gyrotaxis has appeared in the literature. In fact, it may be an oversimplification to model phototaxis in algae in the absence of gravitational bias. We address these issues in this paper by formulating three novel models that incorporate all three taxes within the rational continuum framework of Pedley & Kessler (1990). We take this framework 'as is' and do not attempt to address other research avenues (such as cell-to-cell interactions): we focus squarely on phototaxis. Typically, cells may assimilate elements of each of the three photo-gyrotactic models, but we explore them separately for clarity. The first approach simply models forward or backward cell-swimming speed as a function of light intensity, so that cells attempt to regulate the amount of light they receive photokinetically, thus providing a photokinetic–gyrotactic description. The second approach assumes that the strength of gyrotaxis for each cell varies as a function of light intensity. Such a response may be due to physical variation of the centre-of-mass offset of each cell (central to the mechanism of gyrotaxis), an

equivalent variation of sedimentary torques, or an associated behavioural response. Whatever the root, we shall refer to this reaction as variation of centre-of-mass. The third approach introduces a new torque due to phototaxis in the gyrotactic torque balance description as a function of light intensity or its gradient. The mechanism for such a torque may be due to a reactive flagellar response (Rüffer & Nultsch 1991). In this study, we choose to investigate in detail the green alga *Chlamydomonas augustae* (sometimes also inexactly called *C. nivalis*), which exhibits aspects of all three models; in particular, cells may respond to light by varying their swimming speed in conjunction with re-orientating via a phototactic torque, and associated variations of sedimentary torques. The three models allow a comparative investigation of modelling approaches and an assessment of whether results are robust.

The same methodology for all models is followed, which is based on the analysis of the model by Pedley & Kessler (1990) applied to a layer of finite depth by Bees & Hill (1998) (itself leaning on the analysis of Hill *et al.* 1989). The Fokker–Planck equation is solved and used to calculate the mean cell-swimming direction and find an estimate for the cell-swimming diffusion tensor, both of which are used in the cell conservation equation. Analytical and numerical equilibrium solutions for the case of no-fluid flow are then found, and a linear-stability analysis is conducted.

This paper is structured as follows. The three approaches of combining phototaxis and gyrotaxis are presented in §2, and the main model equations for the most general model are formulated in §3. The Fokker–Planck equation for the cell orientation distribution is solved for the various cases for weak flow in §4. The equilibrium solutions and linear-stability analyses are presented in §5, and in §5.4 asymptotic analyses for deep layers and weak illumination for models A and B are explored. In §6, numerical results for all models are presented and, finally, the models and results are compared and discussed in §7.

2. Modelling photo-gyrotaxis: three approaches

The three model approaches to include phototaxis in the stochastic gyrotaxis model of Pedley & Kessler (1990), denoted models A, B and C, are described as follows. These three models operate at different levels in the system.

2.1. *Model A: photokinesis–gyrotaxis*

Model A is a photokinetic description in which V_s, the magnitude of the cell-swimming velocity multiplied by $+1$ for forward motion and -1 for backward motion, varies as a function of light intensity, I. Cells swim forwards when I is less than the critical intensity, I_c^A, and backwards when $I > I_c^A$. The term photokinesis indicates that there is movement in response to an external light stimulus without orientational bias. On the other hand, gravitaxis and gyrotaxis function as normal, exerting a directional bias; in the absence of gravity, there is no preferred swimming direction and the cells on average neither swim up nor down. In general, the swimming cells do not necessarily move towards or away from the light source, but may display phototactic-like behaviour when the axes of the light source and gravity or shear flow are aligned. This is a somewhat phenomenological modelling approach. For this model, we require the cells to swim at their standard speed in the dark, a zero swimming speed at $I = I_c^A$, and for the cells to swim backwards when the light is too bright. Hence, in the absence of experimental data, for simplicity we choose V_s to be a linear function of I, so that

$$V_s(I) = -\xi\left(I - I_c^A\right), \tag{2.1}$$

where ξ is a constant. Setting $V_s(0) = V_n$, the cell-swimming speed in the dark, gives $\xi = V_n/I_c^A$.

2.2. *Model B: light intensity-dependent centre-of-mass offset*

Model B is a phenomenological description in which the cells act as though their centre-of-mass offset h (the distance between the cell's geometric centre and centre-of-mass) varies with light intensity. This will affect the deterministic–stochastic balance of each cell such that when $|h|$ is large, the cell will swim more deterministically upwards or downwards, and when $|h|$ is small the cell will swim more stochastically. When the cell is at the preferred light intensity, I_c^B, $h = 0$, and there will be no gravitaxis or gyrotaxis, so the cell will move stochastically, with no preferred direction. Note that the critical light intensity does not necessarily take the same value as in model A. Cells swim upwards in the dark, so that $h(I)$ attains its standard value when $I = 0$, and $h = 0$ for $I = I_c^B$. For simplicity with light from above, $h(I)$ is chosen as a linear function of I:

$$h(I) = -\xi\left(I - I_c^B\right), \tag{2.2}$$

where ξ is a constant. As $h(0) = h_n$, the normal centre-of-mass offset in the dark, $\xi = h_n/I_c^B$.

2.3. *Model C: reactive phototactic torque*

In this model, a new effective torque due to phototaxis, $\boldsymbol{L}_p$, is introduced, which alters the torque-balance equation. We propose a general phototactic torque of the form

$$\boldsymbol{L}_p = f(I)\boldsymbol{p} \wedge (\beta_1\boldsymbol{\pi} + \beta_2\nabla I), \tag{2.3}$$

with constants β_1 and β_2, where $f(I)$ is the phototactic strength. Thus, we may investigate both the response of cells to light from an arbitrary global direction, $\boldsymbol{\pi}$, and the possible effects of the cells reacting to local gradients in light intensity, ∇I.

As model C includes a new phototactic torque on top of the gravitational and viscous torques, we require that its additional effects vanish at both $I = 0$ and I_c^C. We choose the simple quadratic functional response $f(I) = F_0 I(I - I_c^C)$, where F_0 is a constant, so that the phototaxis torque, $\boldsymbol{L}_p$, is zero, both when there is no light *and* when the cells are at the critical light intensity, I_c^C. (Note that I_c^C, in general, may take a different value to I_c^A or I_c^B.) The phototaxis torque is self-contained: phototaxis and gyrotaxis are modelled separately and can exist independently; at I_c^C, the cells are still gyrotactic and can swim but the phototactic torque is turned off. Here F_0 is chosen so that between $I = 0$ and $I = I_c^C$ the strength of the torque is positive, such that the cells are biased to swim towards the light under low light conditions. The maximum torque is arbitrarily set to occur at $I_c^C/2$, so that $F_0 = 4f_m/I_c^{C2}$, where f_m is the maximum of $f(I)$. The torque is

$$\boldsymbol{L}_p = -\frac{4f_m}{I_c^2}I\left(I - I_c^C\right)\boldsymbol{p} \wedge (\beta_1\boldsymbol{\pi} + \beta_2\nabla I). \tag{2.4}$$

Different forms for the effective phototactic torque may be explored. Here, we shall consider the effects due to cells responding to light from an arbitrary direction and local gradients in light intensity: for cases I and II, $(\beta_1, \beta_2) = (1, 0)$ and $(0, H/I_s)$, respectively.

In the absence of any data to the contrary, we now set $I_c^A = I_c^B = I_c^C = I_c$, so that the critical light intensity is the same in each model.

3. The continuum description

3.1. *Governing equations*

All three combined photo-gyrotactic models are based on the state-of-the-art model proposed by Pedley & Kessler (1990) for gyrotactic cells (which itself is based on the gravitaxis model of Childress *et al.* 1975). We assume that the sides of the container are sufficiently far apart that the layer effectively is of infinite width and use, for the most part, both rigid upper and lower boundaries. We model the microorganism distribution using a continuous density distribution and prescribe that cells are more dense than the fluid in which they swim. The fluid is assumed to be incompressible and the suspension is modelled as dilute, so cell-to-cell interactions are neglected. We assume that the length scale of the bulk motions is large compared with typical cell spacing and cell size.

Following the rationale for the continuum model of a dilute suspension of swimming gravitactic and gyrotactic cells due to Pedley & Kessler (1990), we assume that the suspension is incompressible and, with a Boussinesq approximation, the momentum equation is

$$\nabla \cdot \boldsymbol{u} = 0, \tag{3.1}$$

$$\rho \left(\frac{\partial \boldsymbol{u}}{\partial t} + (\boldsymbol{u} \cdot \nabla)\boldsymbol{u} \right) = -\nabla p_e + nv\Delta\rho g + \nabla \cdot \Sigma. \tag{3.2}$$

Here, $\boldsymbol{u}(\boldsymbol{x}, t)$ is the fluid velocity, $\Sigma(\boldsymbol{x}, t)$ is the fluid stress tensor, $p_e(\boldsymbol{x}, t)$ is the excess pressure, $n(\boldsymbol{x}, t)$ is the cell concentration, v is the volume of a cell, g is the acceleration due to gravity, and ρ and $\rho + \Delta\rho$ are the densities of the fluid and cells, respectively.

The total number of cells is conserved, so that

$$\frac{\partial n}{\partial t} = -\nabla \cdot [n\boldsymbol{u} + nV_s(I)\langle \boldsymbol{p}(\boldsymbol{u}, I)\rangle - \boldsymbol{D}(\boldsymbol{u}, I) \cdot \nabla n], \tag{3.3}$$

where I denotes light intensity. The first term on the right-hand side of (3.3) is due to advection of the cells by the fluid. The second term is due to cell swimming, where $V_s(I)$ is the mean cell-swimming speed multiplied by $+1/-1$ for forward/backward motion dependent on light intensity, and $\langle \boldsymbol{p}(\boldsymbol{u}, I)\rangle$ is the mean cell-swimming direction. The third term is due to diffusion, where $\boldsymbol{D}(\boldsymbol{u}, I)$ is the cell-swimming diffusion tensor. For sufficiently small cells, the flow is locally linear and then we write $\langle \boldsymbol{p}(\boldsymbol{\Omega}, \boldsymbol{E}, I)\rangle$ and $\boldsymbol{D}(\boldsymbol{\Omega}, \boldsymbol{E}, I)$ for the mean cell-swimming direction and diffusion tensor, respectively, where $\boldsymbol{\Omega}(\boldsymbol{x}, t)$ is the vorticity and $\boldsymbol{E}(\boldsymbol{x}, t)$ is the rate-of-strain tensor.

Consider a cell-swimming direction probability density function, $f(\boldsymbol{p})$, defined on a unit sphere, where the unit vector $\boldsymbol{p} = (\sin\theta\cos\phi, \sin\theta\sin\phi, \cos\theta)^T$ is the cell-swimming direction and the spherical polar angles θ and ϕ are the colatitude measured relative to $\boldsymbol{k}$ and orientation angle in the horizontal plane, respectively. Note that $f(\boldsymbol{p}(\theta, \phi))$ satisfies the Fokker–Planck equation

$$\frac{\partial f}{\partial t} + \nabla_p \cdot (\dot{\boldsymbol{p}} f) = D_r \nabla_p^2 f, \tag{3.4}$$

where D_r is rotational diffusivity, which models randomness in cell orientation due to the intrinsically imperfect cell motion, and the dot indicates a time derivative. Following Pedley & Kessler (1987), and as the cells and their flagella move at very small Reynolds number, we sum all torques, including the new torque due to phototaxis, to obtain an expression for the rate of change of the cell-swimming

Name	Description	Standard values	Units
ρ	Density of fluid	1.0	$\mathrm{gm\,cm^{-3}}$
$\rho + \Delta\rho$	Cell density	1.05	$\mathrm{gm\,cm^{-3}}$
v	Cell volume	5×10^{-10}	$\mathrm{cm^3}$
g	Acceleration due to gravity	10^3	$\mathrm{cm\,s^{-2}}$
μ	Viscosity	10^{-2}	$\mathrm{gm\,cm^{-1}\,s^{-1}}$
V_n	Mean cell-swimming speed	63	$\mathrm{\mu m\,s^{-1}}$
D_0	Diffusivity	5×10^{-5}–5×10^{-4}	$\mathrm{cm^2\,s^{-1}}$
h	Centre-of-mass offset	0–0.5	$\mathrm{\mu m}$
B_n	Gyrotactic reorientation time scale	3.4	s
B_n	As above with flagella	6.3	s
D_r	Rotational diffusivity of cells	0.067	$\mathrm{s^{-1}}$
τ	Direction correlation time	1.3–5	s
$\alpha^\star$	Cellular extinction coefficient	3.7×10^{-7}–6.7×10^{-7}	$\mathrm{cm^2}$

Name	Description/definition	Standard values	Reference
α_0	Cell eccentricity $= (a^2 - b^2)/(a^2 + b^2)$ (a and b are major and minor axes)	0.2–0.31	n.a.
$\alpha_\perp$	Resistance coefficient ($\perp$ to $\boldsymbol{p}$)	6.8	(see Pedley & Kessler 1990)
χ	Scaled light intensity	0–2.7	(3.17)
d	Ratio of layer depth to sublayer depth	20–200	(3.11)
η	Non-dimensional gyrotaxis parameter	0–0.04	(3.19)
κ	Non-dimensional measure of absorption	0–2.0	(3.20)
λ	Deterministic–stochastic parameter	2.2	(3.19)
R	Rayleigh number	0–10^{10}	(3.16)
S_c	Schmidt number	19	(3.16)
ζ	Phototactic torque strength (model C)	0–10	(B 2)

TABLE 1. Parameter descriptions, estimates and references for the green algae *C. augustae*.

direction:

$$\dot{\boldsymbol{p}} = \frac{1}{2B(h(I))}[\bar{\boldsymbol{k}}(I) - (\bar{\boldsymbol{k}}(I) \cdot \boldsymbol{p})\boldsymbol{p}] + \frac{1}{2}\boldsymbol{\Omega} \wedge \boldsymbol{p} + \alpha_0[\boldsymbol{E} \cdot \boldsymbol{p} - \boldsymbol{p}\boldsymbol{p} \cdot \boldsymbol{E} \cdot \boldsymbol{p}], \qquad (3.5)$$

where α_0 is a measure of cell eccentricity (see table 1). Here, the new torque due to phototaxis has been combined with the gravitational torque, so that the upward unit vector, $\boldsymbol{k}$, is replaced by $\bar{\boldsymbol{k}}(I)$, a vector that shall be defined in §§ B.1 and B.2. Furthermore,

$$B(h(I)) = \frac{\mu\alpha_\perp}{2h(I)\rho g}, \qquad (3.6)$$

where $h(I) = -(h_n/I_c)(I - I_c)$ is the centre-of-mass offset dependent on light intensity, μ is fluid viscosity, $\alpha_\perp$ is the dimensionless resistance coefficient for rotation about an axis perpendicular to $\boldsymbol{p}$, and h_n is the centre-of-mass offset in the dark. Likewise, B is the gyrotactic reorientation time scale, a constant in Pedley & Kessler (1990) that may now depend on light intensity, I, via the centre-of-mass offset, h.

In general, the cells affect the flow in ways other than through their negative buoyancy. Pedley & Kessler (1990) determined that the most significant contribution to the bulk stress is due to stresslets associated with the swimming motion of the cells. However, they found that for the linear stability of a dilute uniform suspension, these extra terms did not have a qualitative effect and were relatively small. Here, for simplicity and clarity, we neglect these additional terms; we assume that the suspension is Newtonian, such that $\Sigma = 2\mu\boldsymbol{E}$.

The mean cell-swimming direction, $\langle \boldsymbol{p} \rangle$, is given by

$$\langle \boldsymbol{p} \rangle = \int_S \boldsymbol{p} f(\boldsymbol{p}) \, \mathrm{d}S, \tag{3.7}$$

where S is the unit sphere. We follow Pedley & Kessler (1990) in approximating the cell-swimming diffusion tensor as

$$\boldsymbol{D} \approx D_0 \langle (\boldsymbol{p} - \langle \boldsymbol{p} \rangle)(\boldsymbol{p} - \langle \boldsymbol{p} \rangle) \rangle, \tag{3.8}$$

where D_0 is a diffusion scale, a satisfactory approximation for small flows (see Hill & Bees 2002 and Manela & Frankel 2003 for rigorous approaches to calculate the diffusion tensor using generalized Taylor dispersion theory). Typically, $D_0 = V_n^2 \tau$, where V_n is a constant average cell-swimming speed and τ is the direction correlation time. In addition, for model A, where cell forward–backward swimming speed is a function of light intensity, then, in principle, diffusion should also be modelled as a function of I. However, for simplicity of this phenomenological description, we choose $\boldsymbol{D}$ to be independent of I.

To model the effects of light from above on bioconvection, we use a self-shading model based on that presented by Vincent & Hill (1996) and further explored by Ghorai & Hill (2005). We assume that light scattering and absorption by the medium is weak and can be disregarded (reasonable for shallow layers; but see Ghorai *et al.* 2010). We also assume that the wavelength of the light does not vary across the suspension and the cells are homogeneous and possess the same transmittance of light in all directions, and we disregard multiple scattering. Finally, we assume that the time scale for changes in light intensity as the cell rotates are longer than the time required for the cell to detect those changes. Hence, using the Lambert–Beer law, the light intensity I at a depth z is

$$I(z) = I_s \exp \left\{ -\alpha^\star \int_z^0 n(z) \, \mathrm{d}z \right\}, \tag{3.9}$$

where $\alpha^\star$ is the cellular extinction coefficient (a measure of light absorption per cell), n is the concentration of cells and I_s is the light intensity at the source ($z = 0$). The integral of the concentration between 0 and z is a measure of how much a cell at position z is shaded by the sum of all cells between it and the light source. One might question whether (3.9) would represent the actual intensity perceived by a cell, as the partially shaded eyespot is typically at some non-zero angle to the light source. However, the distribution of helical trajectories of cells will allow some averaging.

The new terms in (3.1)–(3.4) (compared with the gyrotaxis model of Pedley & Kessler 1990) are $V_s(I)$ and $h(I)$, which were previously constants, and $\bar{\boldsymbol{k}}(I)$, which was previously the constant unit vector in the vertical direction, $\boldsymbol{k}$. The models are formulated so that if there is no light, $I = 0$, hence no phototaxis, then $V_s(I) = V_n$, $h(I) = h_n$ and $\bar{\boldsymbol{k}}(I) = \boldsymbol{k}$, and the model equations are the same as in Bees & Hill (1998) and Pedley & Kessler (1990) for gyrotactic and gravitactic cells. Although all models are included in these general photo-gyrotactic model equations, we study each model individually and investigate only one light-dependent term at a time.

Consider a suspension trapped between two rigid horizontal boundaries, H cm apart. As cells tend to form a dense raft of cells at the upper surface, no-slip boundary conditions are typically employed at both boundaries (Bees & Hill 1998). The raft rapidly arises as a monolayer, with cells' flagella sticking to the surface and to each other, and appears to play no further role in bioconvection. Microscope observation of cell trajectories suggests that a zero perpendicular cell flux is the

Name	Definition	Value	Name	Definition	Value
K_1	$\coth \Lambda - \dfrac{1}{\Lambda}$	0.57	J_1	$\dfrac{4}{3}\pi\lambda\mu_\Lambda \sum\limits_{l=0}^{\infty} \Lambda^{2l+1} a_{2l+1,1}$	0.45
K_2	$1 - \coth^2 \Lambda + \dfrac{1}{\Lambda^2}$	0.16	J_2	$\dfrac{4}{5}\pi\lambda\mu_\Lambda \sum\limits_{l=1}^{\infty} \Lambda^{2l} a_{2l,2}$	0.16
K_4	$K_2 - \dfrac{K_1}{\Lambda}$	-0.10	J_4	$\dfrac{4}{3}\pi\lambda\mu_\Lambda \sum\limits_{l=0}^{\infty} \Lambda^{2l+1} \tilde{a}_{2l+1,1}$	-0.23^*
K_5	$-\dfrac{2}{\Lambda}\left[1 + K_2 - \dfrac{4K_1}{\Lambda}\right]$	-0.11	J_5	$\dfrac{4}{5}\pi\lambda\mu_\Lambda \sum\limits_{l=0}^{\infty} \Lambda^{2l} \tilde{a}_{2l,2}$	-0.17^*
K_6	$K_1^2 - 1 + \dfrac{2K_1}{\Lambda}$	N/A	J_6	$\dfrac{16}{5}\pi\lambda\mu_\Lambda \sum\limits_{l=0}^{\infty} \Lambda^{2l} \bar{a}_{2l,2}$	-0.20
K_7	$\dfrac{K_1^2}{\Lambda} + \dfrac{3K_1}{\Lambda^2} - \dfrac{1}{\Lambda}$	N/A	J_7	$\dfrac{4}{3}\pi\Lambda\mu_\Lambda \sum\limits_{l=1}^{\infty} \Lambda^{2l}(z) \hat{a}_{2l,1}$	N/A
K_8	$\dfrac{2}{\Lambda} - \dfrac{2K_1^2}{\Lambda} - \dfrac{6K_1}{\Lambda^2}$	N/A	J_8	$\dfrac{4}{5}\pi\Lambda\mu_\Lambda \sum\limits_{l=0}^{\infty} \Lambda^{2l+1}(z) \hat{a}_{2l+1,2}$	N/A
μ_Λ	$\dfrac{\Lambda}{4\pi \sinh \Lambda}$	0.039			

TABLE 2. The terms K_i and J_i and their corresponding values when $\Lambda = \lambda = 2.2$ and $\alpha_0 = 0.2$. Constants $a_{i,j}$, $\tilde{a}_{i,j}$ and $\bar{a}_{i,j}$ are given in Appendix A. Asterisks indicate values which were wrongly calculated in Pedley & Kessler (1990) (as $J_4 = -0.26$ and $J_5 = -0.13$) and have been corrected here. Here K_4 is from Bees & Hill (1998) as corrected from Pedley & Kessler (1990).

natural choice of a simple boundary condition to use, and is the one employed in the literature (see Hill *et al.* 1989). However, it is possible that the situation may be more complicated (and may depend temporally on the cell biology), although this issue is beyond the scope of the current paper. Thus,

$$\boldsymbol{u} = \boldsymbol{0} \quad \text{and} \quad \boldsymbol{k} \cdot (n(\boldsymbol{u} + V_s(I)\langle \boldsymbol{p}\rangle) - \boldsymbol{D} \cdot \nabla n) = 0 \quad \text{at} \quad z = 0, -H. \quad (3.10)$$

3.2. *Non-dimensionalization of the general model*

The governing equations are non-dimensionalized as in Bees & Hill (1998), where length and time are scaled with H and H^2/D_0, respectively. Note that $V_s(I)$ is non-dimensionalized with the constant cell-swimming speed in the dark, denoted V_n (obtained from Hill & Häder 1997, for *C. augustae*, nee *nivalis*) and $h(I)$ in (3.6) with the centre-of-mass offset in the dark, h_n (the same as h in Bees & Hill 1998). To allow direct comparisons between these results and those of Bees & Hill (1998), we non-dimensionalize n with N, where

$$N = \frac{d\bar{n}}{1 - e^{-d}} \quad \text{and} \quad d = \frac{\bar{K}_1 H V_n}{\bar{K}_2 D_0}, \quad (3.11)$$

which arises from the equilibrium solution (see §5), where $\bar{n}$ is the mean cell concentration and $\bar{K}_1$ and $\bar{K}_2$ are the values of the functions $K_1(\Lambda)$ and $K_2(\Lambda)$, defined in table 2, when $\Lambda = 2.2$ (as is the case in Bees & Hill (1998); from the Fokker–Planck equation in (4.7) and (4.8), see §4). Here d is the ratio of layer depth H to sublayer depth in the gyrotaxis-only problem of Bees & Hill (1998) and can be thought of as a non-dimensional layer depth. When $d \ll 1$ the layer is 'shallow' and when $d \gg 1$ the layer is 'deep'. We non-dimensionalize I using light intensity at the

source, I_s. Hence, put

$$
\left.
\begin{aligned}
&\tilde{x} = \frac{x}{H}, \quad \tilde{n} = \frac{n}{N}, \quad \tilde{\boldsymbol{D}} = \frac{\boldsymbol{D}}{D_0}, \quad \tilde{t} = \frac{t D_0}{H^2}, \quad \tilde{\boldsymbol{u}} = \frac{\boldsymbol{u} H}{D_0}, \quad \tilde{\boldsymbol{\Sigma}} = \frac{\boldsymbol{\Sigma} H^2}{D_0 \mu}, \\
&\tilde{p}_e = \frac{p_e H^2}{\mu D_0}, \quad \tilde{I} = \frac{I}{I_s}, \quad \tilde{V}_s = \frac{V_s}{V_n}, \quad \boldsymbol{\Omega} = \frac{D_0}{H^2}\boldsymbol{\omega}, \quad \boldsymbol{E} = \frac{D_0}{H^2}\mathbf{e} \quad \text{and} \quad \tilde{h} = \frac{h}{h_n},
\end{aligned}
\right\}
$$
(3.12)

where $\boldsymbol{\omega}$ is the dimensionless vorticity and $\mathbf{e}$ the dimensionless rate-of-strain tensor. On dropping tildes, the non-dimensional incompressibility condition (3.1), Navier–Stokes equation (3.2) and cell conservation equation (3.3) become

$$
\nabla \cdot \boldsymbol{u} = 0,
$$
(3.13)

$$
S_c^{-1} \frac{\mathrm{D}\boldsymbol{u}}{\mathrm{D}t} = -\nabla p_e - \gamma n \boldsymbol{k} + \nabla \cdot \Sigma,
$$
(3.14)

$$
\frac{\partial n}{\partial t} = -\nabla \cdot \left[n \left(\boldsymbol{u} + \frac{V_n H}{D_0} V_s(I)\langle \boldsymbol{p} \rangle \right) - \boldsymbol{D} \cdot \nabla n \right],
$$
(3.15)

respectively. Here, the Schmidt number, S_c, and the Rayleigh number, R, are given by

$$
S_c = \frac{\nu}{D_0} \quad \text{and} \quad R = \gamma d, \quad \text{where} \quad \gamma = \frac{N \nu g \Delta\rho H^3}{\nu \rho D_0},
$$
(3.16)

respectively, where ν is the kinematic viscosity; R is a ratio of the buoyancy forces that drive the instability to the viscous forces that inhibit it, and is based on the depth of the full fluid layer as in Hill *et al.* (1989). It has the same definition as in Bees & Hill (1998), allowing comparison of results.

We use the steady-state version of the Fokker–Planck equation, as in Pedley & Kessler (1990), assuming that the time scale for unsteadiness in the flow is large compared to D_r^{-1}. From (3.6), put

$$
B(h(I)) = \frac{B_n}{\tilde{h}(I)}, \quad \text{where} \quad B_n = \frac{\mu \alpha_\perp}{2 h_n \rho g}, \quad \tilde{h}(I) = -(\chi I - 1) \quad \text{and} \quad \chi = \frac{I_s}{I_c}.
$$
(3.17)

Then, non-dimensionalizing the Fokker–Planck equation, and dropping tildes, yields

$$
h(I)\nabla_p \cdot [(\bar{\boldsymbol{k}}(I) - (\bar{\boldsymbol{k}}(I) \cdot \boldsymbol{p}) \cdot \boldsymbol{p}) f] + \eta \nabla_p \cdot [(\boldsymbol{\omega} \wedge \boldsymbol{p}) f]
$$
$$
+ 2\alpha_0 \eta \nabla_p \cdot [(\mathbf{e} \cdot \boldsymbol{p} - \boldsymbol{p}\boldsymbol{p} \cdot \mathbf{e} \cdot \boldsymbol{p}) f] = \lambda^{-1}\nabla_p^2 f, \quad (3.18)
$$

where

$$
\lambda = \frac{1}{2 D_r B_n} \quad \text{and} \quad \eta = \frac{B_n D_0}{H^2},
$$
(3.19)

where η is the dimensionless gyrotaxis parameter. The non-dimensional light intensity is given by

$$
I(z) = \exp\left\{ -\kappa \int_z^0 n(z)\,\mathrm{d}z \right\}, \quad \text{where} \quad \kappa = \alpha^\star H N.
$$
(3.20)

Here κ is a dimensionless measure of light absorption by the cells. Furthermore,

$$
V_s(I) = -\left(\chi \exp\left\{ -\kappa \int_z^0 n(z)\,\mathrm{d}z \right\} - 1 \right),
$$
(3.21)

and the phototaxis torque is $\boldsymbol{L}_p = -4f_m\chi I(\chi I - 1)\boldsymbol{p} \wedge (\beta_1\pi + \beta_2\nabla I)$, where the scalings from ∇I have been incorporated into β_2.

As in Vincent & Hill (1996), we remove the integral by defining

$$m = -\int_z^0 n(z)\,\mathrm{d}z \quad \text{so} \quad n(z) = \frac{\mathrm{d}m}{\mathrm{d}z}. \tag{3.22}$$

The no-flow and no-flux boundary conditions become

$$\boldsymbol{u} = \boldsymbol{0} \quad \text{and} \quad \boldsymbol{k}\cdot\left(n\boldsymbol{u} + \frac{V_n H}{D_0}V_s(I)n\langle\boldsymbol{p}\rangle - \boldsymbol{D}\cdot\nabla n\right) = 0 \quad \text{at} \quad z = 0, -1. \tag{3.23}$$

A further boundary condition is obtained by setting $z = 0$ in (3.22), so that

$$m = 0 \quad \text{at} \quad z = 0. \tag{3.24}$$

So far, the model has been formulated for any general swimming green algae species. Table 3.1 lists standard parameter values that will be used in all three models for *C. augustae*. Most of these values are the same as in Bees & Hill (1998), to allow comparisons between the models, and come from Pedley & Kessler (1990), Jones, Le Baron & Pedley (1994), Hill & Häder (1997) and Hill *et al.* (1989). Typically, the cells have a diameter of $10\,\mu\mathrm{m}$, with an average distance between cells of $100\,\mu\mathrm{m}$, while the length scale for pattern formation is larger, at around 0.1–0.5 cm.

4. Solution of the Fokker–Planck equation

For the case of small flows, Pedley & Kessler (1990) obtained a solution of the gyrotactic Fokker–Planck equation (corrected in Bees & Hill 1998). For model A, only the forward–backward swimming speed varies and thus we may quote the solutions from these references. For models B and C, however, there are additional terms in the solution. We shall briefly outline the procedure for obtaining solutions to (3.18) for model A (for which the Fokker–Planck equation is the same as for no illumination): $\langle\boldsymbol{p}\rangle$ and $\boldsymbol{D}$ will be determined. The additional terms due to phototaxis for models B and C are then calculated. The results are summarized in table 3.

4.1. *Solution of the Fokker–Planck equation for model A*

Here, we set $h(I) = 1$ and $\bar{k}(I) = k$. The derivatives in (3.18) are in orientation space, and so $\boldsymbol{k}$, $\boldsymbol{\omega}$ and $\boldsymbol{e}$ are considered constants. The non-dimensional Fokker–Planck equation simplifies (Pedley & Kessler 1990) to

$$(\boldsymbol{k}\cdot\nabla_p f - 2(\boldsymbol{k}\cdot\boldsymbol{p})f) + \eta\boldsymbol{\omega}\cdot(\boldsymbol{p}\wedge\nabla_p f) + 2\eta\alpha_0[\boldsymbol{p}\cdot\boldsymbol{e}\cdot\nabla_p f - 3\boldsymbol{p}\cdot\boldsymbol{e}\cdot\boldsymbol{p}f] = \lambda^{-1}\nabla_p^2 f. \tag{4.1}$$

Consider the equilibrium state of no-flow, denoted by superscript 0, where $\boldsymbol{u} = \boldsymbol{\omega} = \boldsymbol{0}$, $\boldsymbol{e} = \boldsymbol{0}$, $f = f^0$ and $m = m^0$. By writing $\boldsymbol{p} = (\sin\theta\cos\phi, \sin\theta\sin\phi, \cos\theta)$, where θ is the colatitude measured relative to $\boldsymbol{k}$ and ϕ is the cell orientation angle in the horizontal plane, and $\boldsymbol{k} = (0, 0, 1)$, then

$$\frac{1}{\sin\theta}\frac{\partial}{\partial\theta}\left(\sin\theta\frac{\partial f^0}{\partial\theta}\right) + \frac{1}{\sin^2\theta}\frac{\partial^2 f^0}{\partial\phi^2} = -\Lambda\left(\sin\theta\frac{\partial f^0}{\partial\theta} + 2f^0\cos\theta\right), \tag{4.2}$$

where, for model A, the general function $\Lambda(z)$ is identically equal to the constant λ (it will be redefined for models B and C). Assuming axial symmetry and applying the normalization condition $\int_S f^0\,\mathrm{d}S = 1$, where S is the surface of a unit sphere, then

$$f^0 = \mu_\Lambda e^{(\Lambda\cos\theta)}, \quad \text{where} \quad \mu_\Lambda = \frac{\Lambda}{4\pi\sinh(\Lambda)}. \tag{4.3}$$

Model $\Lambda(z)$		Extra terms in $\langle p \rangle$ (4.7)	Extra terms in D (4.8)
A	λ	None	None
B	$\lambda(1 - \chi\, \mathrm{e}^{\kappa m})$	$\lambda \chi \kappa m^1 \mathrm{e}^{\kappa m^0} K_6 k$	$\lambda\chi\kappa m^1 \mathrm{e}^{\kappa m^0}\,[K_7(ii + jj)$ $+ (K_8 - 2K_1 K_6)kk]$
C, I	$\lambda(1 - \zeta\chi\, \mathrm{e}^{\kappa m^0}$ $\times (\chi\, \mathrm{e}^{\kappa m^0} - 1))$	$\lambda \zeta \chi \kappa m^1 \mathrm{e}^{\kappa m^0}$ $\times (2\chi\, \mathrm{e}^{\kappa m^0} - 1)K_6 k$	$\lambda\zeta\chi\kappa m^1 \mathrm{e}^{\kappa m^0}(2\chi\, \mathrm{e}^{\kappa m^0} - 1)$ $\times\, [K_7(ii + jj) + (K_8 - 2K_1 K_6)kk]$
C, II	$\lambda(1 - C^0)$	$-\dfrac{\lambda c^0}{\Lambda}\left(J_7 + \dfrac{2J_1}{\lambda}\right)[G_1^1 i + G_2^1 j]$ $+ \lambda C^1 K_6 k$	$-\dfrac{\lambda c^0}{\Lambda}(J_8 + \dfrac{2J_2}{\lambda} - K_1(J_7 + \dfrac{2J_1}{\lambda}))$ $\times\, [G_1^1(ik + ki) + G_2^1(jk + kj)]$ $+ \lambda C^1 [K_7(ii + jj) + (K_8 - 2K_1 K_6)kk]$

TABLE 3. A summary of the components of $\langle p \rangle$ and D that arise from the solution to the Fokker–Planck equation. For every model, this consists of the solution for the gyrotactic-only case of Pedley & Kessler (1990) as in (4.7) and (4.8), with Λ defined herein, along with any additional terms stated here. For each contribution to $\langle p \rangle$ due to phototaxis, the corresponding expressions for the diffusion tensor are indicated. Model C parameters are defined in Appendix B.

Substituting (4.3) into (3.7) and (3.8) gives

$$\langle p \rangle^0(z) = (0, 0, K_1(\Lambda))^{\mathrm{T}}, \quad \text{and} \quad D^0 = \begin{pmatrix} \dfrac{K_1(\Lambda)}{\Lambda} & 0 & 0 \\ 0 & \dfrac{K_1(\Lambda)}{\Lambda} & 0 \\ 0 & 0 & K_2(\Lambda) \end{pmatrix}, \quad (4.4)$$

where $K_1(\Lambda)$ and $K_2(\Lambda)$, for $\Lambda = \lambda$, are defined in table 2.

Consider an infinitesimal perturbation, denoted by superscript 1, such that

$$u = \epsilon u^1, \quad \omega = \epsilon \omega^1, \quad e = \epsilon e^1, \quad f = f^0 + \epsilon f^1 \quad \text{and} \quad m = m^0 + \epsilon m^1, \quad (4.5)$$

where $0 < \epsilon \ll 1$. Equation (4.1) at order ϵ is

$$\frac{1}{\sin\theta}\frac{\partial}{\partial\theta}\left(\sin\theta\frac{\partial f^1}{\partial\theta}\right) + \frac{1}{\sin^2\theta}\frac{\partial^2 f^1}{\partial\phi^2} - \Lambda\left(k \cdot \hat{\theta}\frac{\partial f^1}{\partial\theta} - 2\cos\theta f^1\right)$$
$$= \eta\lambda\left(\omega^1 \cdot p \wedge \hat{\theta}\frac{\partial f^0}{\partial\theta} + 2\alpha_0 p \cdot e^1 \cdot \hat{\theta}\frac{\partial f^0}{\partial\theta} - 6\alpha_0 p \cdot e^1 \cdot p f^0\right). \quad (4.6)$$

The solution f^1 can be obtained in terms of the associated Legendre polynomials (Pedley & Kessler 1990). Then, to $O(\epsilon)$,

$$\langle p \rangle = \langle p \rangle^0 + \epsilon\langle p \rangle^1 = \begin{pmatrix} 0 \\ 0 \\ K_1 \end{pmatrix} + \epsilon\left[\eta J_1\begin{pmatrix} \omega_2 \\ -\omega_1 \\ 0 \end{pmatrix} - 2\alpha_0\eta\begin{pmatrix} e_{13}J_4 \\ e_{23}J_4 \\ \frac{3}{2}e_{33}K_4 \end{pmatrix}\right], \quad (4.7)$$

$$D = D^0 + \epsilon D^1 = \begin{pmatrix} \dfrac{K_1}{\Lambda} & 0 & 0 \\ 0 & \dfrac{K_1}{\Lambda} & 0 \\ 0 & 0 & K_2 \end{pmatrix} + \epsilon\left[\eta(J_2 - J_1 K_1)\begin{pmatrix} 0 & 0 & \omega_2 \\ 0 & 0 & -\omega_1 \\ \omega_2 & -\omega_1 & 0 \end{pmatrix} - 2\alpha_0\eta\right.$$

$$\times \begin{pmatrix} -\frac{3}{4}e_{33}K_5 + \frac{1}{4}(e_{11} - e_{22})J_6 & \frac{1}{2}e_{12}J_6 & e_{13}(J_5 - K_1 J_4) \\ \frac{1}{2}e_{12}J_6 & -\frac{3}{4}e_{33}K_5 - \frac{1}{4}(e_{11} - e_{22})J_6 & e_{23}(J_5 - K_1 J_4) \\ e_{13}(J_5 - K_1 J_4) & e_{23}(J_5 - K_1 J_4) & \frac{3}{2}e_{33}(K_5 - 2K_1 K_4) \end{pmatrix} \Bigg].$$

$$(4.8)$$

Definitions for the constants K_i and J_i (which depend on Λ) and values of these constants when $\Lambda = \lambda = 2.2$ (from the range computed by Pedley & Kessler 1990) are shown in table 2. An error in the calculation of the values J_4 and J_5 was found; the corrected values are $J_4 = -0.23$ and $J_5 = -0.17$. However, this only makes a small quantitative difference (5.7 % error in the critical Rayleigh number).

4.2. *Amendments to the solution of the Fokker–Planck equation: model B*

The Fokker–Planck equation (3.18) for model B, where $\bar{k}(I) = k$ and $h(I)$ is defined in (3.17), becomes

$$\lambda(1 - \chi e^{\kappa m(z)})(k \cdot \nabla_p f - 2(k \cdot p)f) + \eta \lambda \omega \cdot (p \wedge \nabla_p f)$$
$$+ 2\eta \lambda \alpha_0 [p \cdot e \cdot \nabla_p f - 3p \cdot e \cdot pf] = \nabla_p^2 f. \qquad (4.9)$$

Collecting terms at zeroth order yields (4.2) with

$$\Lambda(z) = \lambda\big(1 - \chi e^{\kappa m^0(z)}\big). \qquad (4.10)$$

The contributions to $\langle p \rangle$ and D are the same as before but with non-constant $K_i(\Lambda(z))$.

At first order, (4.9) provides an equation similar to (4.6) but with $\Lambda(z)$ as in (4.10), and an additional term on the right-hand side:

$$-\lambda \chi \kappa m^1 e^{\kappa m^0} \left(k \cdot \hat{\theta} \frac{\partial f^0}{\partial \theta} - 2\cos\theta f^0\right). \qquad (4.11)$$

Expressions for $\langle p \rangle$ and D can be obtained from (4.7) and (4.8), on replacing λ with $\Lambda(z)$, and a solution associated with (4.11). Hence, suppose

$$f^1 = \lambda \chi \kappa \mu_\lambda m^1 e^{\kappa m^0} \mathscr{H}(\theta, z). \qquad (4.12)$$

Substituting (4.12) into (4.6) with the term (4.11), and putting $x = \cos\theta$, we obtain

$$((1 - x^2)\mathscr{H}')' - \Lambda((1 - x^2)\mathscr{H})' = -[e^{\Lambda x}(1 - x^2)]', \qquad (4.13)$$

with normalization condition $\int_{-1}^{1} \mathscr{H}(x, z)\, dx = 0$. Hence,

$$\mathscr{H}(x, z) = e^{\Lambda x}\,(K_1(z) - x), \qquad (4.14)$$

and we obtain the contributions to $\langle p \rangle$ and D due to the new term for phototaxis:

$$\langle p \rangle^1 = \lambda \chi \kappa m^1 e^{\kappa m^0} \begin{pmatrix} 0 \\ 0 \\ K_6 \end{pmatrix}, \quad \text{and} \quad D^1 = \lambda \chi \kappa m^1 e^{\kappa m^0} \begin{pmatrix} K_7 & 0 & 0 \\ 0 & K_7 & 0 \\ 0 & 0 & K_8 - 2K_1 K_6 \end{pmatrix},$$

$$(4.15)$$

where $K_6(z)$, $K_7(z)$ and $K_8(z)$ are defined in table 2. As $\chi \to 0$, these terms vanish.

4.3. *Amendments to the solution of the Fokker–Planck equation: model C*

Model C is somewhat more complex. We outline the solution process in Appendix B.

4.4. *Summary of results of the Fokker–Planck equation*

Table 2 shows the definitions of all $K_i(\Lambda(z))$ and $J_i(\Lambda(z))$ and corresponding values for the case $\Lambda = \lambda = 2.2$, as used in the gyrotaxis-only case in Pedley & Kessler (1990). Table 3 summarizes the extra contributions due to phototaxis to the mean cell-swimming direction and diffusion tensor given in (4.7) and (4.8), respectively, where for each model the definition of $\Lambda(z)$ used in the functions K_i and J_i is also provided. (Note that the limit of terms as $\Lambda \to 0$ is well defined, as can be observed by expanding with respect to small Λ.)

5. Linearized equations

5.1. *Equilibrium solutions*

First, consider an equilibrium solution for the case of no-fluid flow, $\boldsymbol{u} = \boldsymbol{0}$, such that $n = n(z)$. We shall integrate the cell conservation equation (3.15) and apply boundary conditions (3.23) and (3.24).

For model A, where $V_s(I) = V_s$, $h(I) = 1$ and $\tilde{\boldsymbol{k}}(I) = \boldsymbol{k}$, the equilibrium solution is governed by

$$\frac{\mathrm{d}^2 m(z)}{\mathrm{d}z^2} - d\left(1 - \chi\,\mathrm{e}^{\kappa m(z)}\right)\frac{\mathrm{d}m(z)}{\mathrm{d}z} = 0. \tag{5.1}$$

For models B and C, $V_s(I) = 1$ in (3.15) and the equilibrium solution satisfies

$$\frac{\mathrm{d}^2 m(z)}{\mathrm{d}z^2} - \frac{d\bar{K}_2}{\bar{K}_1}\frac{K_1(\Lambda(z))}{K_2(\Lambda(z))}\frac{\mathrm{d}m(z)}{\mathrm{d}z} = 0, \tag{5.2}$$

where $K_i(\Lambda(z))$ are determined from the solution to the Fokker–Planck equation and $\Lambda(z)$ is defined for each model in table 3.

The normalization condition $\int_{-1}^{0} n(z)\mathrm{d}z = \bar{n}/N$ (i.e. in dimensional units $\int_{-H}^{0} n(z)\,\mathrm{d}z = \bar{n}H$) provides $m = (\mathrm{e}^{-d} - 1)/d$ at $z = -1$. We also have the boundary condition that $m = 0$ at $z = 0$. Note that if $\chi = 0$, then the equilibrium solution for all models is an exponential distribution for $n(z)$, as for the gyrotaxis-only case (Bees & Hill 1998).

5.2. *Analytic equilibrium solution for the case of weak absorption in models A and B*

As in Vincent & Hill (1996), if we assume the case of weak absorption, so that $0 < \kappa \ll 1$ and I is close to I_c, then we can find an analytical equilibrium solution. Hence, to first order in κ for model A, (5.1) becomes

$$\frac{\mathrm{d}n}{\mathrm{d}z} + \frac{d}{I_c}\left(I_s\left[1 - \kappa\int_z^0 n(z)\,\mathrm{d}z\right] - I_c\right)n(z) = 0. \tag{5.3}$$

The critical intensity I_c occurs at position $z = -C$ $(0 \leqslant C \leqslant 1)$ for an individual cell for the vertically uniform concentration profile $n = 1$. Thus, $I_c = I_s\mathrm{e}^{-\kappa\int_{-c}^{0} 1\mathrm{d}z} = I_s(1 - \kappa C) + O(\kappa^2)$, so that $(\mathrm{d}n/\mathrm{d}z) - d\kappa[\int_z^0 n(z)\,\mathrm{d}z - C]n(z) = 0$. The unique solution is

$$n(z) = \frac{\dfrac{K^2}{2G_1}\left[(K^2/G_1^2) - C^2\right]\mathrm{sech}^2(Kz/2)}{[(K/G_1) + C\tanh(Kz/2)]^2}, \tag{5.4}$$

where $G_1 = d\kappa$ is a constant defined for convenience (see model B below) and K is a constant obtained from the transcendental equation

$$\left(\frac{K^2}{G_1^2} - C^2 + d^{-1}(1 - \mathrm{e}^{-d})C\right)\tanh\left(\frac{K}{2}\right) - \frac{d^{-1}(1 - \mathrm{e}^{-d})K}{G_1} = 0 \tag{5.5}$$

on using the non-dimensional normalization condition. This solution was originally obtained by Kamke (1967) and is similar to the solution presented in Ghorai & Hill (2005), a corrected version of results in Vincent & Hill (1996), except that we use different non-dimensionalization and boundary conditions.

For model B, (4.10) can be expanded to yield

$$\Lambda = \lambda\kappa\left(\int_z^0 n(z)\,\mathrm{d}z - C\right) + O(\kappa^2). \tag{5.6}$$

Furthermore, $K_1(\Lambda)/K_2(\Lambda) = \Lambda + O(\Lambda^3)$, and thus to order κ,

$$\frac{\mathrm{d}n}{\mathrm{d}z} - \frac{d\bar{K}_2}{\bar{K}_1}\lambda\kappa\left[\int_z^0 n(z)\,\mathrm{d}z - C\right]n(z) = 0. \tag{5.7}$$

This has the same form as (5.2), except with different constants outside the bracket, and the solution is given by (5.4), where $G_1 = (d\bar{K}_2/\bar{K}_1)\lambda\kappa$ and K is a constant obtained from the transcendental equation (5.5).

5.3. *Governing equations for linear-stability analysis*

Consider a small perturbation from the equilibrium solution such that $\boldsymbol{u} = \epsilon\boldsymbol{u}^1$, $n = n^0 + \epsilon n^1$, $m = m^0 + \epsilon m^1$, $\langle\boldsymbol{p}\rangle = \langle\boldsymbol{p}\rangle^0 + \epsilon\langle\boldsymbol{p}\rangle^1$, $p_e = p_e^0 + \epsilon p_e^1$ and $\boldsymbol{D} = \boldsymbol{D}^0 + \epsilon\boldsymbol{D}^1$, where $\epsilon \ll 1$, and the superscript 0 indicates the zeroth-order, no-flow equilibrium solution and 1 indicates the first-order perturbation. On substituting the perturbations into (3.13), (3.14) and (3.22), and collecting terms of order ϵ gives

$$\nabla\cdot\boldsymbol{u}^1 = 0, \qquad n^1 = \frac{\mathrm{d}m^1}{\mathrm{d}z}, \tag{5.8}$$

$$S_c^{-1}\frac{\partial\boldsymbol{u}^1}{\partial t} = -\nabla p_e^1 - \gamma n^1\boldsymbol{k} + \nabla^2\boldsymbol{u}^1. \tag{5.9}$$

Take the divergence of (5.9) and the Laplacian of the third component and combine to give

$$S_c^{-1}\frac{\partial}{\partial t}\left(\nabla^2 u_3^1\right) = \nabla^4 u_3^1 - \gamma\nabla^2 n^1 + \gamma\partial_3\partial_3 n^1. \tag{5.10}$$

Consider the normal modes

$$u_3^1 = U(z)\exp[\mathrm{i}(lx + my) + \sigma t], \quad n^1 = \Phi(z)\exp[\mathrm{i}(lx + my) + \sigma t],$$
$$m^1 = M(z)\exp[\mathrm{i}(lx + my) + \sigma t], \tag{5.11}$$

where σ is the growth rate of the perturbation and $k = \sqrt{l^2 + m^2}$ is the horizontal wavenumber, which is related to the non-dimensional wavelength, λ_0, via $\lambda_0 = 2\pi/k$. Substituting into (5.10) gives

$$\left(\frac{\sigma}{S_c} + k^2 - \frac{\mathrm{d}^2}{\mathrm{d}z^2}\right)\left(k^2 - \frac{\mathrm{d}^2}{\mathrm{d}z^2}\right)U = -Rd^{-1}k^2\Phi, \tag{5.12}$$

where the Rayleigh number R is defined in (3.16).

In the following sections, it is more convenient to perform the linear analysis for each model separately, although it will be kept brief to avoid unnecessary repetition.

5.3.1. *Model A*

For model A, $h(I) = 1$, $\bar{\boldsymbol{k}} = \boldsymbol{k}$ and the full solution to the Fokker–Planck equation is the same as in Pedley & Kessler (1990): $\langle \boldsymbol{p} \rangle$ and $\boldsymbol{D}$ are given by (4.7) and (4.8), respectively, with $\Lambda = \lambda$ (a constant) and K_i and J_i constants $\forall i$ in table 3.

Expanding the cell conservation equation (3.15) gives

$$
\begin{aligned}
\frac{\partial n^1}{\partial t} = -\partial_3 n^0 u_3^1 - \frac{d\bar{K}_2}{\bar{K}_1} \Big[& \partial_i((1 - \chi e^{\kappa m^0})n^1)\langle \boldsymbol{p} \rangle_i^0 + \partial_3((1 - \chi e^{\kappa m^0})n^0)\langle \boldsymbol{p} \rangle_3^1 \\
& + (1 - \chi e^{\kappa m^0})n^0 \partial_i \langle \boldsymbol{p} \rangle_i^1 - \partial_i(\chi \kappa m^1 e^{\kappa m^0} n^0)\langle \boldsymbol{p} \rangle^0 \Big] + D_{ij}^0 \partial_i \partial_j n^1 + D_{33}^1 \partial_3 \partial_3 n^0 \\
& + \partial_3 n^0 \partial_i D_{i3}^1,
\end{aligned}
\tag{5.13}
$$

where $V_s(I)$ has been expanded to give $V_s(I) = 1 - \chi e^{\kappa m^0} - \epsilon \chi \kappa m^1 e^{\kappa m^0} + O(\epsilon^2)$. Note that in this case $\Lambda = \lambda$ constant, so $\bar{K}_1 = K_1(\Lambda) = K_1(\lambda)$, defined in table 3, so from here on we drop the bar on constants K_1 and K_2 for model A. From the solution for the Fokker–Planck equation in (4.7) and (4.8), we have

$$
\partial_i \langle \boldsymbol{p} \rangle_i^1 = -\eta(J_1 + \alpha_0 J_4)\nabla^2 u_3^1 + \eta \alpha_0(2J_4 - 3K_4)\partial_3 \partial_3 u_3^1, \tag{5.14}
$$

$$
\begin{aligned}
\partial_i D_{i3}^1 = & -\eta(J_2 - J_1 K_1 + \alpha_0(J_5 - K_1 J_4))\nabla^2 u_3^1 \\
& + \eta \alpha_0 \left(2(J_5 - K_1 J_4) - 3(K_5 - 2K_1 K_4) \right) \partial_3 \partial_3 u_3^1.
\end{aligned}
\tag{5.15}
$$

Substituting (5.14) and (5.15) into (5.13) gives

$$
\begin{aligned}
\frac{\partial n^1}{\partial t} = & \left\{ \frac{K_1}{\lambda}(\partial_1 \partial_1 + \partial_2 \partial_2) + K_2 \partial_3 \partial_3 \frac{dK_2}{K_1}K_1 \left[(1 - \chi e^{\kappa m^0})\partial_3 + \partial_3(1 - \chi e^{\kappa m^0}) \right] \right\} n^1 \\
& + \left\{ \left[\partial_3 n^0 H_3 - \frac{dK_2 H_1}{K_1}(1 - \chi e^{\kappa m^0})n^0 \right] \nabla^2 + \left[\partial_3 n^0 H_4 - \frac{dK_2 H_2}{K_1}(1 - \chi e^{\kappa m^0})n^0 \right] \partial_3 \partial_3 \right. \\
& \left. - \partial_3 n^0 + 3\alpha_0 \eta \left[\partial_3 \left(\frac{dK_2}{K_1}(1 - \chi e^{\kappa m^0})n^0 \right) K_4 - (K_5 - 2K_1 K_4)\partial_3^2 n^0 \right] \partial_3 \right\} u_3^1 \\
& + dK_2 \chi \kappa \partial_3 \left(m^1 e^{\kappa m^0} n^0 \right),
\end{aligned}
\tag{5.16}
$$

where $H_1 = -\eta(J_1 + \alpha_0 J_4)$, $H_2 = \eta \alpha_0(2J_4 - 3K_4)$, $H_3 = -\eta(J_2 - J_1 K_1 + \alpha_0(J_5 - K_1 J_4))$ and $H_4 = \eta \alpha_0(2(J_5 - K_1 J_4) - 3(K_5 - 2K_1 K_4))$. Substituting the normal modes in (5.11) into the cell conservation equation (5.16), and writing the resulting expression so that direct comparisons can be made with the equivalent gyrotaxis-only expression in Bees & Hill (1998), gives

$$
\begin{aligned}
\left(P_V \frac{d^2}{dz^2} - P_H k^2 - \sigma - P_V d P_Q(z)\frac{d}{dz} + 2P_V d\chi \kappa P_R(z) \right) \Phi(z) + P_V d\chi \kappa P_M(z)M(z) \\
= \left(\frac{dn^0}{dz} - \eta P_5(z;d)\frac{d^2}{dz^2} - \eta P_6(z;d)\frac{d}{dz} + \eta P_7(z;d)k^2 \right) U(z),
\end{aligned}
\tag{5.17}
$$

Name	Definition	Value
A_1	$J_1 K_1 - J_2 + \alpha_0(-J_5 + K_1 J_4 + 2(J_5 - K_1 J_4) - 3(K_5 - 2K_1 K_4))$	0.0977
A_2	$J_1 - \alpha_0(J_4 - 3K_4)$	0.442
A_3	$3\alpha_0 K_4$	-0.06
A_4	$3\alpha_0(K_5 - 2K_1 K_4)$	0.0054
A_5	$-(J_2 - J_1 K_1 + \alpha_0(J_5 - K_1 J_4)$	0.0929
A_6	$-J_1 - \alpha_0 J_4$	-0.398
P_V	K_2	0.16
P_H	$\dfrac{K_1}{\lambda}$	0.26

TABLE 4. Definitions of A_i, P_V and P_H, which are constants in model A only, and their values when $\lambda = 2.2$ and $\alpha_0 = 0.2$ in model A.

where P_i are functions of z such that

$$
\left.
\begin{aligned}
&P_Q(z) = \left(1 - \chi e^{\kappa m^0}\right), \quad P_R(z) = e^{\kappa m^0} n^0, \quad P_M(z) = e^{\kappa m^0}\left(\frac{\mathrm{d}n^0}{\mathrm{d}z} + \kappa(n^0)^2\right), \\
&P_5(z;d) = A_1 \frac{\mathrm{d}n^0}{\mathrm{d}z} + \frac{dK_2}{K_1} A_2\left(1 - \chi e^{\kappa m^0}\right)n^0, \\
&P_6(z;d) = \frac{dK_2}{K_1} A_3 \frac{\mathrm{d}}{\mathrm{d}z}\left(\left(1 - \chi e^{\kappa m^0}\right)n^0\right) - A_4 \frac{\mathrm{d}^2}{\mathrm{d}z^2}n^0 \\
&\qquad\quad = \frac{dK_2}{K_1} A_3\left[-\chi\kappa e^{\kappa m^0}(n^0)^2 + \left(1 - \chi e^{\kappa m^0}\right)\frac{\mathrm{d}n^0}{\mathrm{d}z}\right] - A_4 \frac{\mathrm{d}^2 n^0}{\mathrm{d}z^2}, \\
&P_7(z;d) = A_5 \frac{\mathrm{d}n^0}{\mathrm{d}z} - \frac{dK_2}{K_1} A_6\left(1 - \chi e^{\kappa m^0}\right)n^0,
\end{aligned}
\right\} \tag{5.18}
$$

and the definitions of the functions A_1 to A_6, and P_H and P_V are stated in table 4, with values when $\Lambda = \lambda$. Here, $n^0 = n^0(z)$ and $m^0 = m^0(z)$. For $\chi = 0$, these equations are exactly the same as the linear-stability equations in Bees & Hill (1998) for the gyrotaxis-only case; for $\chi = 0$, we find identical neutral curves. The terms involving $P_R(z)$ and $P_M(z)$ are new.

The boundary conditions (3.23) and (3.24) become

$$
\left.
\begin{aligned}
&U = \frac{\mathrm{d}U}{\mathrm{d}z} = M = \frac{\mathrm{d}\Phi}{\mathrm{d}z} - d(1 - \chi)\Phi = 0 \quad \text{on} \quad z = 0, \\
&U = \frac{\mathrm{d}U}{\mathrm{d}z} = \frac{\mathrm{d}\Phi}{\mathrm{d}z} - d\left(1 - \chi e^{\kappa m^0}\right)\Phi + d\kappa\chi e^{\kappa m^0} n^0 M = 0 \quad \text{on} \quad z = -1.
\end{aligned}
\right\} \tag{5.19}
$$

5.3.2. *Models B and C*

We present the derivation of the linear-stability equations for models B and C (cases I and II) in Appendix C due to their complexity.

5.4. *Asymptotic analysis for a deep layer and weak illumination in models A and B*

We may derive asymptotic results for a deep layer, $d^{-1} \ll 1$, and weak illumination, $\chi \ll 1$, using techniques similar to Bees & Hill (1998). Using standard parameter values from table 3.1, we find $d \approx 435H$ (or $d \approx 113H$ for $\tau = 5$). Hence, for an average experimental depth of 4 mm, $d = 174$, which is sufficiently large for deep layer analysis to apply. Here, shallow layers ($d \ll 1$) are not investigated as they are outside the region of experimental interest. van Dyke (1968) presented a full

description of the ideas involved in this analysis, where an outer solution far from the upper boundary is matched to an inner solution.

First, an asymptotic equilibrium solution must be found, after which the asymptotic solutions for the linear-stability equations with appropriate boundary conditions are calculated for outer and inner solutions. These are then matched, and an expression for the Rayleigh number as a function of wavenumber is established via solvability conditions. The solution process is outlined and the results are presented in Appendix D.

6. Numerical analysis for models A, B and C and discussion of model results

For each model, solutions to the equilibrium and linear-stability equations were obtained numerically. A fourth-order finite-difference numerical scheme called 'NRK' (Cash & Moore 1980) was employed, which iterates using a Newton–Raphson–Kantorovich algorithm. Initial guesses for solutions for the cell concentration Φ, fluid velocity U and Rayleigh number R were tried and modified until good convergence was achieved. The solution for the first wavenumber k was then employed as the trial solution for the next value of k, so that as long as the steps between wavenumbers were sufficiently small, a smooth neutral curve could be traced out. Providing a good guess for the Rayleigh number of the mode-one solution was important and the asymptotics helped provide a suitable range. Convergence was always found for at least six significant figures. When the parameter d, the non-dimensional layer depth, was large and χ small, the size of mesh was particularly important. For this reason, and to allow comparisons with Bees & Hill (1998), we scale the equilibrium and linear-stability equations using $z_1 = dz$, so that the domain is defined by $-d \leqslant z_1 \leqslant 0$, and we use a variety of grids to acquire smooth solutions. Solutions were deemed acceptable when a doubling and/or tripling of the nodes did not alter the form of the converged solutions; up to 513 grid points were used to obtain proper convergence, although this was not always necessary and the programme often found solutions with less. Convergence was hard to obtain for more extreme parameter values, such as for large χ or η. In these cases, the parameter in question had to be increased by a small amount each time and the solution for a particular k was saved and used as the initial guess for the increased value of the parameter in the next run.

On the neutral stability curves, the real part of the growth rate is zero: $\mathrm{Re}(\sigma) = 0$. If the imaginary part of σ is also zero, then the perturbation is stationary or non-oscillatory. However, if $\mathrm{Im}(\sigma) \neq 0$ then overstable, or oscillatory, solutions exist; such solutions were found here. For each choice of the key parameters, there are an infinite number of branches of the neutral curve $R^n(k)$, where $n = 1, 2, 3, \ldots$. We look for the branch on which R has its minimum, at (k_c, R_c). For $k_c \neq 0$ and a Rayleigh number just greater than the critical value, the most rapidly growing disturbance from equilibrium generally has wavenumber k_c. (An instability with wavenumber zero for $k_c = 0$ is never observed as the mode has a zero growth rate.) Solutions may consist of stacked convection cells, and are termed 'mode n' if there are n convection cells (or if U changes sign $n - 1$ times). In this study, the critical wavenumber was usually on the mode-one $R^1(k)$ branch.

The large number of parameters make it difficult to investigate the full parameter space. In this paper, we wish predominantly to explore the balance between phototaxis and gyrotaxis. For this reason, we fix $\lambda = 2.2$ and $\alpha_0 = 0.2$, as in Pedley & Kessler (1990). We vary the wavenumber, k, the gyrotaxis parameter, η, the phototaxis parameter, χ, the strength of the phototactic torque, ζ, and the measure of the
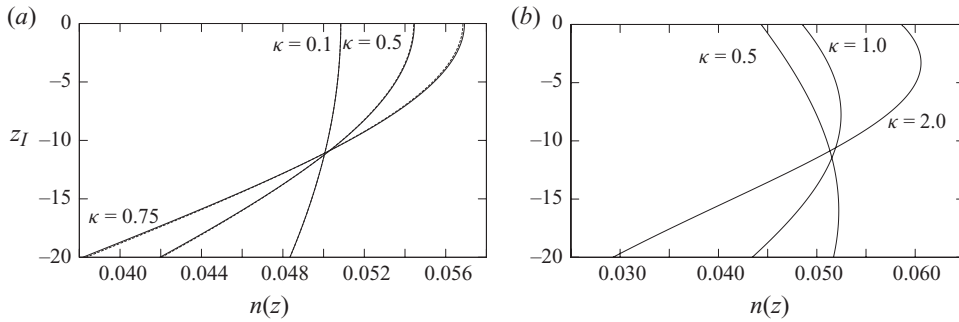
FIGURE 2. Model A equilibrium solutions. (*a*) Comparison between numerical (solid) and analytical (dashed) profiles, where $d = 20$, $\chi = 1.2$ and κ varies. The non-dimensional coordinate z is scaled with non-dimensional layer depth d. The agreement between methods is excellent, even for large κ. (*b*) Numerical profiles for $d = 20$, $\chi = 1.02$ and $\kappa = 0.5$, 1.0 and 2.0.

strength of absorption of the cells, κ, using specific values to illustrate the general behaviour of the system. Where possible, parameters are chosen so that comparisons with Bees & Hill (1998) and Vincent & Hill (1996) can be made. Note that the results in Vincent & Hill (1996) are valid only for the case of weak absorption, $\kappa \ll 1$, and there are errors such that solutions are only correct when C, the location of the sublayer, is at the upper or lower boundary or located at the mid-point of the layer.

In the following sections, equilibrium profiles and stability analyses will be presented and compared for the three complementary models of photo-gyrotaxis as a function of light intensity, I. To reiterate, model A varies forward–backward swimming speed as a function of I, model B allows the cell to adjust its centre-of-mass offset with I, and model C applies a phototactic torque due to I (case I) and its gradient (case II).

6.1. *Equilibrium solutions*

In figure 2(*a*), numerical and analytical equilibrium solutions are presented for model A when $d = 20$, $\chi = 1.2$ and κ varies. Although the analytical solution should be valid only for small κ, we see excellent agreement between numerical and analytical results up to $\kappa = 0.75$ and indeed beyond. Similar agreement is found for model B (not shown). Figure 3 presents the profiles where $\kappa = 1.2$ and $d = 20$ and χ varies. Equilibrium solutions for models A and B are very similar and show the same qualitative trends. The case $\chi = 0$ is equivalent to there being no light in the system ($I_s = 0$) and results in a gyrotaxis-only exponential equilibrium profile with maximum at $z = 0$, as in Bees & Hill (1998) and Hill *et al.* (1989). As χ is increased to $\chi = 1$ (or $I_c = I_s$), the maximum concentration remains at $z = 0$ but the distribution is less peaked than for $\chi < 1$, because the swimming speed is slightly reduced (note that this is due to the linear assumption for $V_s(I)$). For $\chi = 1$, if there was just one cell in the layer, then it could be at any vertical position and still get the optimum light, I_c. It is shading due to the presence of the cells that determines the position of maximum concentration. For $\chi > 1$, the cells near the light source have too much light and start to swim downwards (by swimming backwards in model A or acting as if they are 'top-heavy' in model B), whereas the cells further down do not get sufficient light, due to shading, and swim upwards. This results in a concentrated sublayer at equilibrium located below the upper boundary; a gravitationally stable layer overlies an unstable one. The concentration profile has the largest spread and smallest peak when the maximum concentration is located at $z = -d/2$, and is symmetric (also
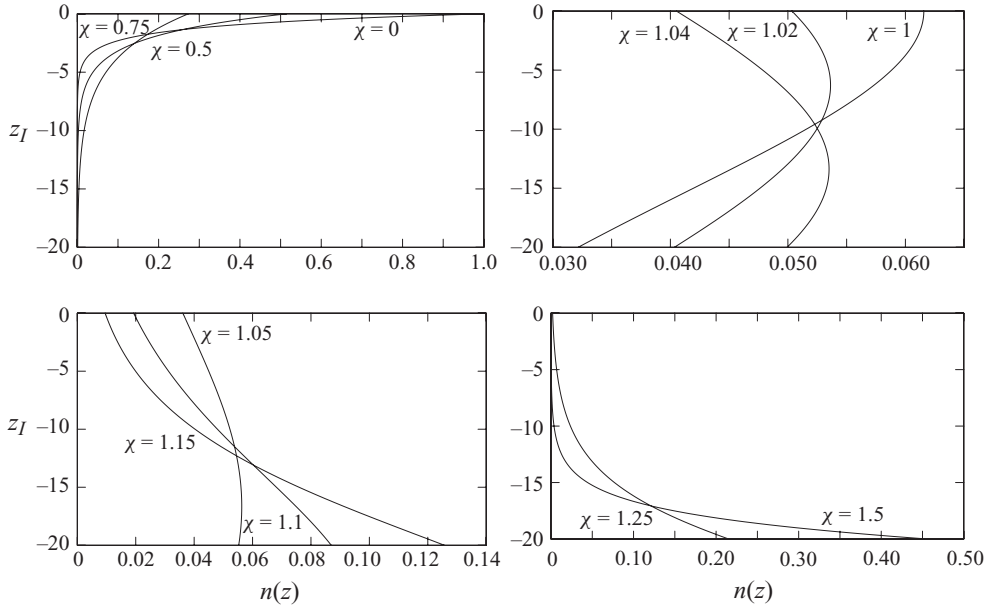
FIGURE 3. Concentration profiles for the equilibrium solution in model A, where $d = 20$, $\kappa = 1.2$ and χ varies. Qualitatively similar solutions were found for model B (not shown).

found in Ghorai & Hill 2005). When χ is large, most cells swim downwards and the distribution is approximately exponential with a maximum at $z = -d$.

Figure 2(b) for model A shows that for $\chi = 1.02$, increasing κ above one causes the maximum of the equilibrium profile to move upwards and become more peaked, which is the opposite effect to increasing χ. This is because increased absorption causes more shading of the cells lower down in the layer, which induces those cells to swim upwards. Large κ also makes solutions less sensitive to changes in χ, so that larger changes in χ are needed to move the peak of $n(z)$.

For model C, case I, we consider illumination from above, so that $\pi = \mathbf{k}$. In this case, the model equations are very similar to those for model B, except that the function of I multiplying the first term of the Fokker–Planck equation differs ((4.9) and (B 1)). If we denote this function by $g(I)$ in both cases, then $g(I) = (1 - \chi I)$ for model B and $g(I) = (1 - \zeta \chi I(\chi I - 1))$ for model C. Note that the parameter ζ is not present in models A and B. To allow some qualitative comparison between models B and C, we fix ζ so that the functions $g(I)$ in each model have the same gradient at $g(I) = 0$, which gives $\zeta = 0.236$. The model results are qualitatively insensitive to different values of ζ.

Figure 4 presents equilibrium solutions for model C, case I, for $d = 20$, $\kappa = 1.0$ and various values of χ. Results are qualitatively similar to models A and B. However, a larger value of χ is required to push the maximum of the equilibrium solution away from $z = 0$, particularly for smaller values of ζ. Furthermore, the concentration at $z = 0$ is greater for $\chi = 0.5$ than $\chi = 0$, which is the opposite of models A and B, and is a result of the additive gravitational and phototactic torques.

Equilibrium solutions for model C, case II, are presented in figure 5, where $\chi = 2$ (so $I_s > I_c$), for various values of ζ. The concentration maximum moves down as ζ is increased (similar to increasing χ in the other models), but the profile is asymmetric. For this model, cells respond to local gradients in light intensity resulting from local
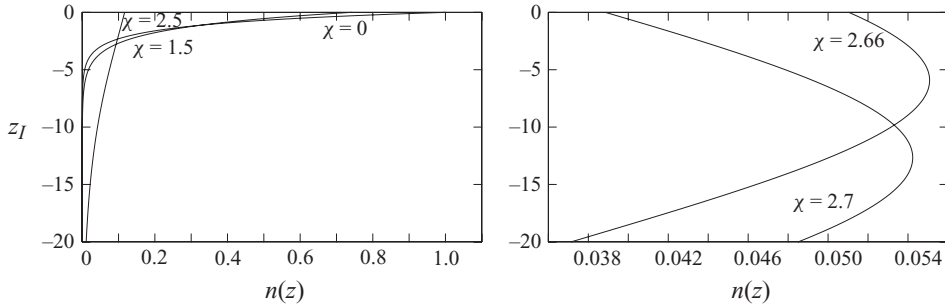
FIGURE 4. Concentration profiles for the equilibrium solution in model C, case I, where $d = 20$, $\kappa = 1.0$, $\zeta = 0.236$ and χ varies.
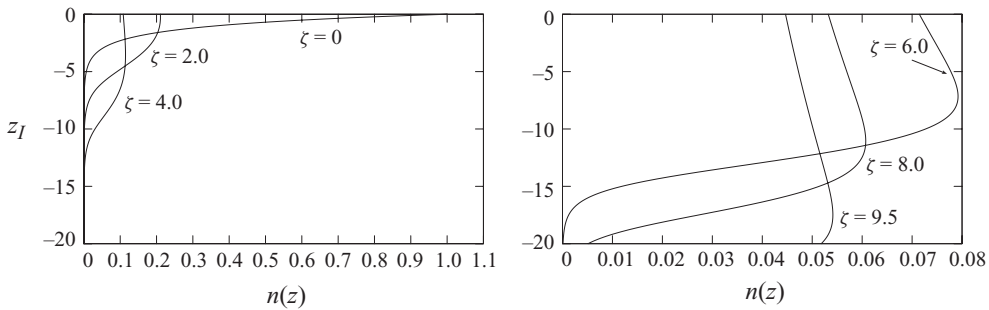

FIGURE 5. Concentration profiles for the equilibrium solution for model C, case II, where $d = 20$, $\kappa = 1.2$, $\chi = 2.0$, $d^2\eta = 4$ and ζ varies.

absorption by the cells; with few cells there is no significant gradient in I and gravitaxis dominates. Furthermore, when the phototaxis torque is strong ($\zeta > 9$), with $\chi > 1$, steady state obtains a balance between negatively phototactic cells responding to ∇I, the necessary local presence of cells to generate significant ∇I, and gravitaxis, all mediated by diffusion; large negative gradients in cell concentration are not supported at steady state, and the profile tends towards something more uniform. Trends in the equilibrium solutions as χ varies (for constant ζ) are qualitatively the same as those for case I.

6.2. *Stability: asymptotic and numerical*

In this section, numerical results are first presented for models A–C (case I) as results are similar; repetition is avoided when possible. We go on to explore mechanisms for oscillatory solutions. Model C, case II, results are presented separately as there are qualitative differences. The main focus of this work is to investigate the effects of changing the phototaxis and gyrotactic balance, using the parameters χ, ζ and η.

6.2.1. *Models A–C (case I)*

Figure 6 presents asymptotic and numerical neutral stability curves for a deep layer ($d^{-1} \ll 1$), where $\chi = d^{-1}$, $\kappa = 1$ and $d = 200$ for model A (model B results are summarized in table 5). Good agreement is found between asymptotics and numerics when $k \leqslant O(1)$, with closer curves for smaller values of $d^2\eta$ and larger d, as expected. The numerics and asymptotics both show the same trend for $k \ll 1$ as η is increased from $d^2\eta = 0$. The numerical results for $k \geqslant O(1)$ show that for increasing η, the neutral curve dips, destabilizing the system and producing a non-zero critical wavenumber for sufficiently large η.

Model	d	$d^2\eta$	$d\chi$	k	R_c numerical	R_c asymptotics
A	40	2	0	0.1	3.16×10^6	3.08×10^6
A	40	2	1	0.1	2.89×10^6	2.84×10^6
A	200	2	0	0.1	1.67×10^9	1.67×10^9
A	200	2	1	0.1	1.64×10^9	1.64×10^9
A	200	2	2	0.1	1.61×10^9	1.61×10^9
A	200	0	1	0.1	8.58×10^8	8.63×10^9
A	200	4	1	0.1	1.79×10^{10}	1.89×10^{10}
B	200	0	1	0.1	8.51×10^8	8.50×10^8
B	200	2	1	0.1	1.57×10^9	1.57×10^9
B	200	4	1	0.1	1.05×10^{10}	1.03×10^{10}

TABLE 5. Summary of numerical and asymptotic results for a deep layer with weak illumination, where $\kappa = 1$. Otherwise, standard parameters were used.
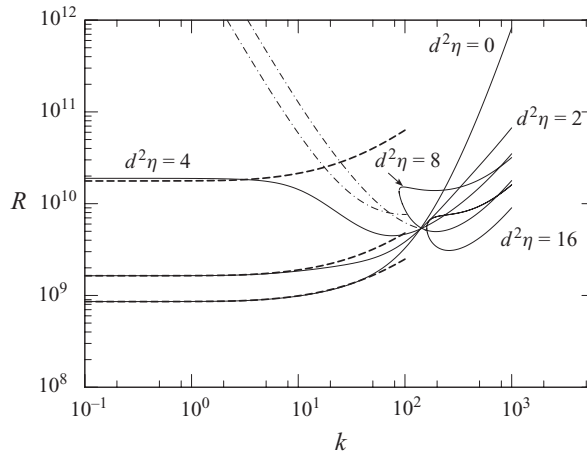
FIGURE 6. Asymptotic (dashed) and numerical (solid) curves of neutral stability for model A, where $d = 200$, $\kappa = 1$ and $\chi = d^{-1}$. The five curves are $d^2\eta = 0$, 2, 4, 8 and 16. Oscillatory branches (numerical) are dot-dashed.

For $d^2\eta > 4$, the Rayleigh number of the neutral curve becomes large for small k: the value of η for which this first occurs can be established from (D 16), which provides

$$\eta_c = \frac{d^{-2}}{P_5 - P_6}. \tag{6.1}$$

For $\lambda = 2.2$ and $\alpha = 0.2$, $d^2\eta_c = 4.2$, consistent with the numerical results (figure 6).

On setting $d^2\eta = 2$ and varying $d\chi < 2$, good agreement is found between asymptotic and numerical results, with closer matches found for $d = 200$ compared with $d = 40$ (table 5). Larger values of χ destabilize the system (note that the χ term in the asymptotic expansion in (D 16) is negative). For $\chi = 0$, there is no light and all models are the same as the gyrotaxis-only model of Bees & Hill (1998): for a range of parameters, we find identical neutral stability curves. In this no-light case, we conclude that small wavenumber instabilities are caused by overturning at the upper boundary and large wavenumber instabilities by gyrotaxis. In their simplified model,

d	$d^2\eta$	χ	κ	k_c	R_c	d	$d^2\eta$	χ	κ	k_c	R_c
20	2	0	1.2	2.44	2.30×10^5	20	64	1.03	1.2	6.74	2.09×10^6
20	2	0.5	1.2	0.0	5.20×10^4	20	0	0.5	1.2	0.0	4.78×10^4
20	2	1.0	1.2	0.0	2.48×10^5	20	16	0.5	1.2	3.70	8.40×10^4
20	2	1.04	1.2	4.88*	2.83×10^7	20	64	0.5	1.2	8.54	5.78×10^4
20	4	0	1.2	7.56	4.27×10^5	20	8	0.1	1.2	12.1	3.70×10^5
20	4	1.0	1.2	0.00	2.47×10^5	20	8	0.5	1.2	2.12	6.74×10^4
20	4	1.04	1.2	5.36*	2.86×10^7	20	8	1.0	1.2	0.0	2.44×10^5
20	0	1.03	1.2	2.79	3.62×10^6	20	8	1.04	1.2	6.72*	2.78×10^7

TABLE 6. Summary of the linear-stability results for model B, for critical wavenumber, k_c, and Rayleigh number, R_c, for $\lambda = 2.2$ and $\alpha_0 = 0.2$. The asterisks indicate mode-two solutions.
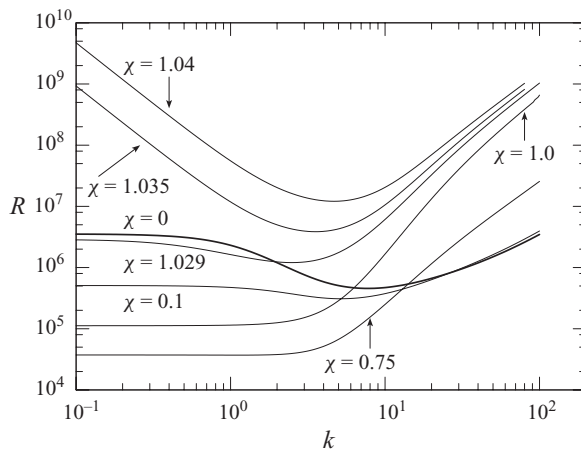
FIGURE 7. Curves of neutral stability for model A, where $d = 20$, $\kappa = 1.2$, $d^2\eta = 2$ and χ varies. The bold line is the special case $\chi = 0$, i.e. no phototaxis.

Vincent & Hill (1996) found looped neutral curves with mode-two sections for weak phototaxis when the position of the sublayer, denoted C, was close to the upper boundary (albeit with slightly flawed analysis). Such solutions were not found here.

Varying χ between $0 \leqslant \chi \leqslant 1.04$ and $0 \leqslant \eta \leqslant 64$ for models A and B, when $d = 20$ and $\kappa = 1.2$, always gave qualitatively similar results and so curves in this section are shown and discussed in detail only for model A (model B results are summarized in table 6). Figure 7 displays results for a range of χ values for $d^2\eta = 4$, where the bold line is the neutral curve for $\chi = 0$ and is the only curve that can be directly compared with Bees & Hill (1998). As $\chi < 1$ is increased from zero (and the equilibrium sublayer is located at $z = 0$), the neutral curve is at first destabilized for small wavenumbers and stabilized for larger wavenumbers, leading to $k_c = 0$. This destabilization of small k indicates that there is a region which causes the critical wavenumber to be zero when it was previously non-zero for the gyrotaxis-only case (see figure 8). The broader equilibrium profile of cells at the upper boundary associated with phototaxis for $0 < \chi < 1$ permits greater fluid flow associated with emergent overturning instabilities, even though the maximum gradient (which occurs at the no-slip boundary) is slightly reduced. However, the gyrotactic instability for large wavenumbers is not dependent on the boundary, and so large wavenumbers due to gyrotaxis are not destabilized. Hence, mostly small wavenumbers are destabilized. As χ increases further, the spread
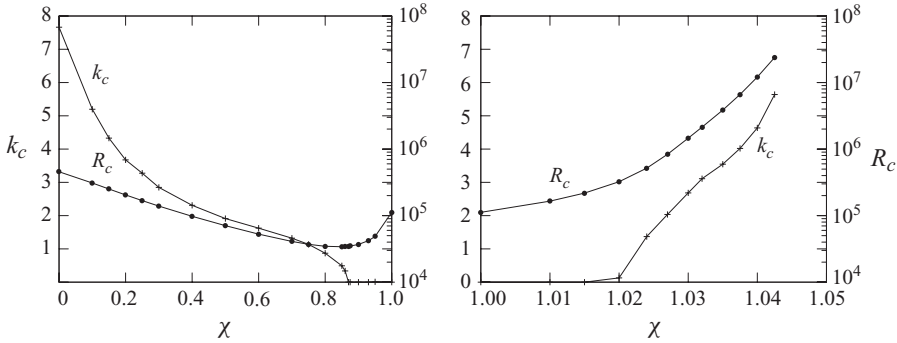
FIGURE 8. Plots of the critical Rayleigh number (circles) and critical wavenumbers (crosses)
for model A, where $d = 20$, $\kappa = 1.2$, $d^2\eta = 4$ and χ varies.
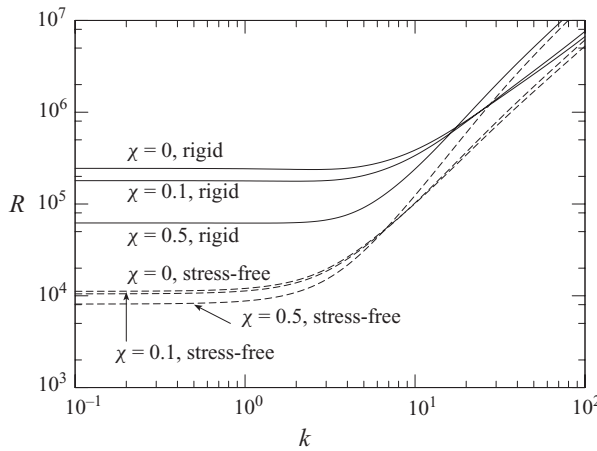

FIGURE 9. Comparison of neutral stability curves for the rigid (solid) and the stress-free
(dashed) boundary conditions for model A, where $d = 20$, $d^2\eta = 2$, $\kappa = 1.2$, and $\chi = 0.0$, 0.1
and 0.5.

of cells at equilibrium also increases, and gradients drop sufficiently to stabilize the
system. This explanation is supported by the fact that for the same model with
a stress-free boundary at $z = 0$, the system is destabilized less than that for the
rigid boundary (as demonstrated in figure 9; the stress-free boundary condition is
$d^2U/dz^2 = 0$ at $z = 0$).

The appearance of the stable region overlying an unstable region at equilibrium as
$\chi > 1$ increases further naturally stabilizes the system for all wavelengths, increasing
R_c. There is a direct relationship between the size of the unstable region and the
stability of the system. When $\chi \geqslant 1.02$ for $d^2\eta = 2$, or $\chi \geqslant 1.03$ for $d^2\eta = 4$, the Rayleigh
number at every wavenumber is larger than for the case $\chi = 0$; all wavenumbers are
stabilized, compared to the gyrotaxis-only model, for χ sufficiently large. Similarly, in
Vincent & Hill (1996), R_c also increased as the sublayer at equilibrium moved further
down the fluid layer, because the effect of destabilization away from the boundary
was offset by the increasingly large stable region. Similar effects were also discussed
by Veronis (1963), Matthews (1988) and Whitehead & Chen (1970) for thermal
instability and convection of a thin fluid layer bounded by stable stratification. The
decrease in size of the unstable layer as χ increases means that it is harder for
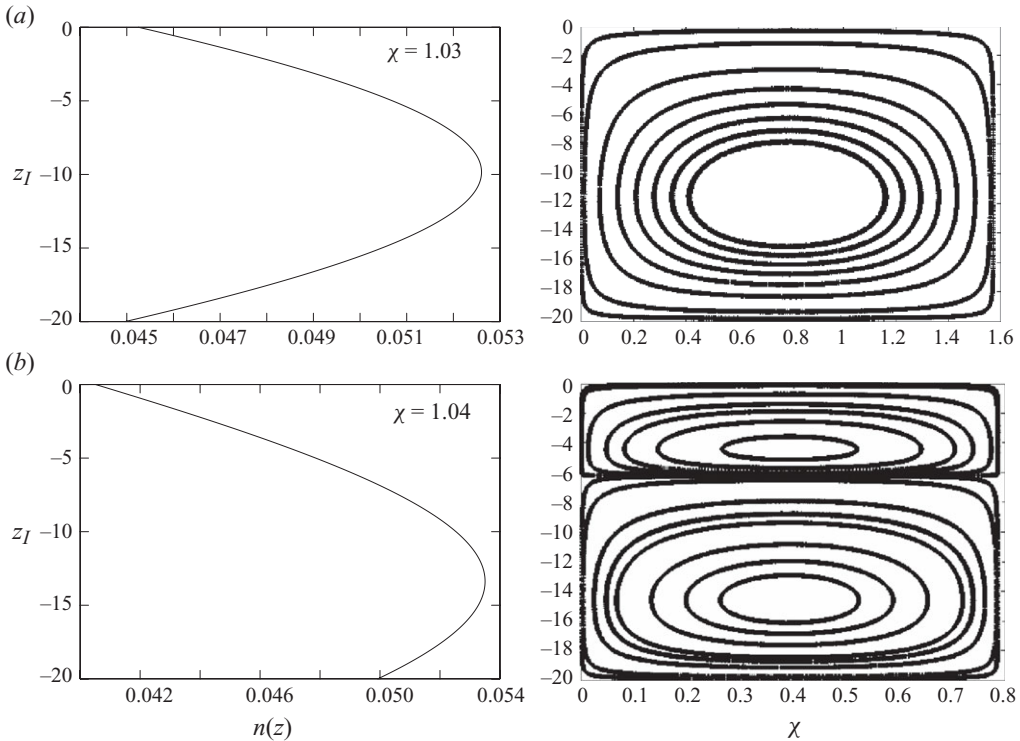
FIGURE 10. Equilibrium solutions and streamlines for model A, where $d = 20$, $\kappa = 1.2$ and $d^2\eta = 4$. (a) $\chi = 1.03$, $k = k_c = 2.68$; (b) $\chi = 1.04$, $k = k_c = 4.75$.

fluid to circulate. This leads to large wavelengths stabilizing more rapidly than small wavelengths, resulting in a dip forming on the neutral curve and a non-zero critical wavenumber for sufficiently large χ. Thus, for models A and B, and for every d and η, if χ is sufficiently large there exists a non-zero value of the critical wavenumber, k_c. As χ increases, the system drives smaller and smaller wavelength instabilities in the shrinking unstable layer, so that the critical wavenumber increases from $k_c = 0$ with $\chi > 1$. Figure 8 summarizes these results.

For very large χ, when the concentrated layer of cells is at the bottom of the suspension, we find purely gyrotactic instabilities (which do not require a density gradient).

For all values of η investigated in models A and B, the critical wavenumber k_c becomes mode-two for sufficiently large χ. For $d^2\eta = 4$ and $\chi = 1.03$, figure 10 indicates that at equilibrium there is a stable layer overlying an unstable layer but the solution at k_c is mode-one (and is also mode-one for $0.1 < k < 10$). Thus, penetrative convection has occurred, where the unstable layer drives fluid motion in the stable layer. However, as χ increases and the stable region increases in size, the energy required for the instabilities to penetrate the stable region becomes too great, and a mode-two instability results (e.g. for $\chi = 1.04$ the solution is mode-two at k_c).

The effects of varying η for the case of $d = 20$ and weak illumination, where $\chi = 0.5$, and strong illumination, where $\chi = 1.03$, are shown in figure 11. For $\chi = 0.5$, where the maximum of the equilibrium concentration is at $z = 0$, figure 11(a) shows that increasing $d^2\eta$ from zero stabilizes small wavenumbers and destabilizes large wavenumbers. The results for $\chi = 1.03$, where the peak concentration occurs midway
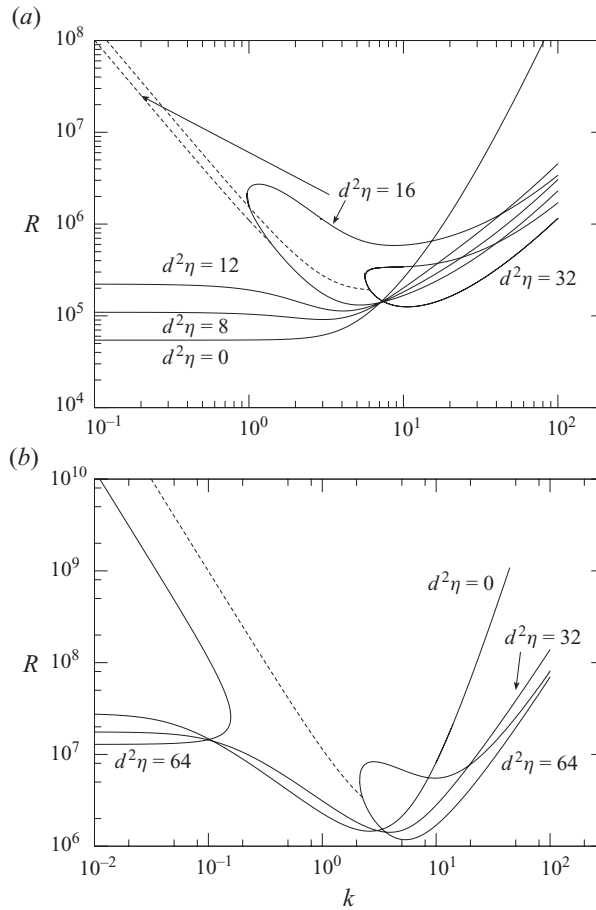
Figure 11. Curves of neutral stability for model A, where $d = 20$, $\kappa = 1.2$ and η varies. Dashed lines are oscillatory solutions: (a) $\chi = 0.5$ and (b) $\chi = 1.03$.

through the layer, are somewhat different. In figure 11(b), the initial wavelength when $d^2\eta = 0$ is non-zero, and little difference is found between the neutral curves for $d^2\eta \leqslant 32$. This shows that for strong illumination (large χ), large values of η are required to have a substantial effect on the system. For $d^2\eta > 32$, large and small wavenumbers are destabilized, as is the case when $\chi = 0.5$. For all χ, there is a non-zero critical wavenumber k_c for $d^2\eta$ sufficiently large, or all $d^2\eta$ if χ is sufficiently large, and k_c increases and R_c decreases as η increases (so that the system is destabilized compared with the case $d^2\eta = 0$). This is consistent with the gyrotaxis-only case in Bees & Hill (1998).

For models A and B, when $d^2\eta \geqslant 16$ for $\chi = 0.5$, and $d^2\eta \geqslant 64$ for $\chi = 1.03$, the neutral curves break into two sections, which turn back on themselves to form loops. The lower branches of these loops have mode-one solutions for all k, but this smoothly adjusts to a mode-two as the loops turn into the upper branch, with the second, smaller, convection cell at the top of the layer for $\chi = 0.5$ and the bottom of the layer for $\chi = 1.03$. These looped solutions were not found in Bees & Hill (1998), although they do exist for the gyrotaxis-only case and similar solutions were found in the phototaxis-only model (Vincent & Hill 1996). The mode-one section of the neutral
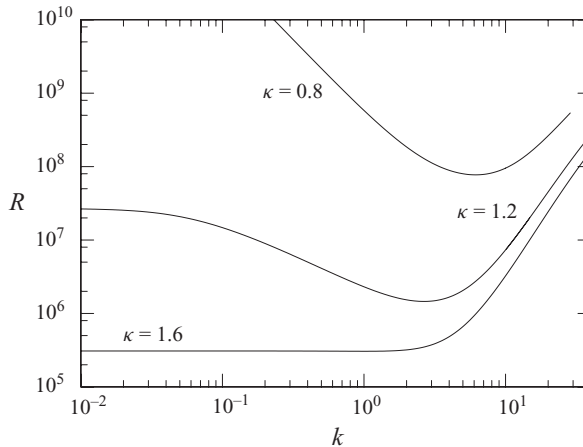
FIGURE 12. Curves of neutral stability for model A, where $d = 20$, $\chi = 1.03$, $d^2\eta = 2$ and $\kappa = 0.8$, 1.2 and 1.6.

curve for small k was found for $d^2\eta = 64$ when $\chi = 1.03$, but was only partially found for $d^2\eta \geqslant 16$ for $\chi = 0.5$ and so is not shown in figure 11.

Oscillatory solutions were found for $d^2\eta \geqslant 16$ when $\chi = 0.5$ and $d^2\eta \geqslant 64$ when $\chi = 1.03$ in both models A and B. Neutral curves that loop back on themselves were always found to have oscillatory solutions with a single oscillatory branch bifurcating from the stationary branch. In all cases investigated, the oscillatory branch did not have a smaller minimum than the stationary branch. For the early deterministic model of gyrotaxis, Hill *et al.* (1989) found oscillatory solutions, thought to be due to the interaction of gyrotaxis and fluid shear close to the rigid upper boundary. Ghorai & Hill (2005) also reported oscillatory solutions in the phototaxis-only model. We shall discuss the mechanisms for overstability in more detail in §6.2.2.

The linear-stability results for increasing κ when $d = 20$, $\chi = 1.03$ and $d^2\eta = 2$ show similar trends to decreasing χ, as shown in figure 12, where R_c and k_c both decrease as a function of increasing κ. This is expected because κ and χ also have opposite effects on the equilibrium solutions, as described in §6.1.

Figure 13 shows neutral curves corresponding to the equilibrium solutions in figure 4 for model C, case I, where $d^2\eta = 4$ and $\zeta = 0.236$ (as described in §6.1). As $\chi < 1$ increases from 0, small wavenumbers are rapidly stabilized, and the non-zero critical wavenumber increases. This is because of the increasing concentration maximum at the rigid upper boundary at equilibrium when $0 < \chi < 1$ compared to $\chi = 0$ (see §6.1), which permits less fluid flow associated with any emergent overturning instability. This stabilization is the opposite to the destabilization for $\chi < 1$ found in models A and B, and is a consequence of the fact that cells can still swim gyrotactically at the critical light intensity in model C (see §2.3).

If χ is increased above $\chi = 1.0$, the maximum of the equilibrium profile decreases and the system is destabilized as the greater spread of cells away from the boundary permits greater fluid flow associated with overturning. This trend was found for increasing χ from zero in models A and B. In model C, when the light is sufficiently bright (large χ) and the phototactic torque strong (large $\zeta\chi$), cells near the light source receive too much light and swim downwards. This results in stabilization of all wavenumbers when $\chi > 2.5$. Small wavenumbers are stabilized more than large wavenumbers, resulting in a non-zero critical wavenumber that increases as a function
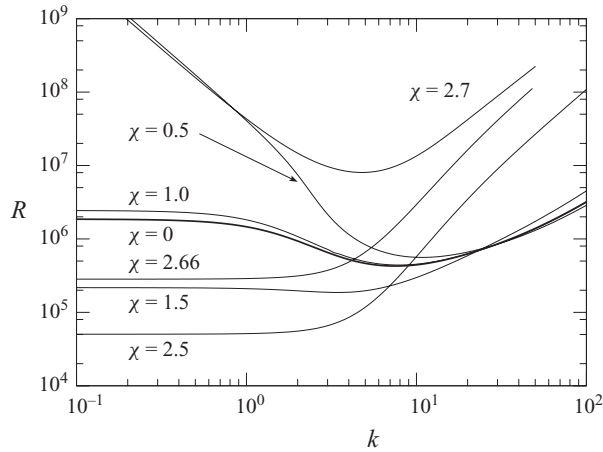
FIGURE 13. Curves of neutral stability for model C, case I, where $d = 20$, $\kappa = 1.0$, $d^2\eta = 4$ and χ varies. We choose $\zeta = 0.236$, so that the gradient at $g(I) = 0$ is the same as in model B.

of χ (as above for models A and B). For $\zeta = 0.236$ in model C, larger values of χ are required for this stabilization compared with models A and B because both a strong phototactic torque and bright light are necessary to move the maximum of the equilibrium profile away from the upper boundary.

6.2.2. *The mechanisms for overstability in models A and B*

For large η for both models A and B, oscillatory branches of the neutral curves were found for all χ, associated with looped stationary branches. Oscillatory solutions occur when there is competition between a stabilizing and a destabilizing process. Hill *et al.* (1989) found that overstability can occur in a suspension of purely gyrotactic algae using an early deterministic model, as long as the upper boundary of the layer is rigid. In this case, there is a shear layer at each boundary associated with the circulation rolls. Hence, there is a net viscous torque on the cells near each downwelling separatrix such that they swim at an angle to the vertical away from the downwelling regions. If the gyrotaxis is sufficiently strong, then there will be a drift of cells away from plume precursors at the upper boundary towards upwelling zones. This could reverse the direction of the circulation and thus cause overstability. We hypothesize that this is also the mechanism for overstability in models A and B when $0 < \chi \leqslant 1$, since the peak of the equilibrium concentration profile occurs at $z = 0$ in all cases.

For $\chi > 1$, oscillatory solutions cannot be explicitly attributed to the effect of the upper boundary, since the maximum of the cell concentration distribution occurs some distance below it. Indeed, for the pure upswimming model, Ghorai & Hill (2005) determined that oscillatory solutions resulted from the entrainment and accumulation of cells, due to penetrative convection, in regions that opposed the original circulation. We hypothesize that oscillatory solutions that arise for sufficiently large η and $\chi > 1$ are due to the particular combination of phototaxis and gyrotaxis, as follows. Unstable density gradients below the subsurface concentration maximum can lead to Rayleigh–Taylor instabilities with gyrotactically focused, descending plumes of cells that can induce penetrative convection in the overlying stable region. However, cells at the top of the plumes may have too much light. In model A, phototaxis leads cells to swim backwards in order to avoid the light, even though they may be gyrotactically
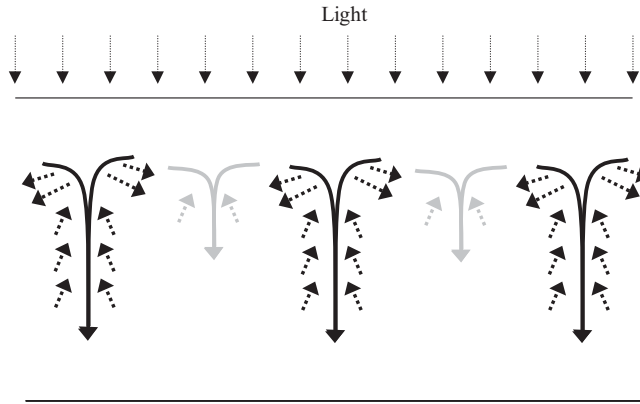
FIGURE 14. Schematic diagram of how oscillations arise for photo-gyrotactic cells. Initial and secondary instabilities are shown by black and grey, respectively, and dashed lines represent swimming cell orientations and solid lines fluid flow. When an instability develops, gyrotactic focusing is involved. However, cells at the top of the plume receive too much light and thus swim away from plumes. Secondary plumes can form between the primary plumes, and may reverse the flow.

orientated to point towards the plume. In model B, phototaxis causes the cells to become effectively top heavy, and they photo-gyrotactically re-orientate so that their swimming motion is directed away from the downwelling fluid. In both models, cells swim away from the concentrated downwelling fluid at an angle to the vertical, defocusing the plumes at the top, thus providing the opportunity for secondary plumes to form between the original structures, damped by swimming diffusion (figure 14). These resultant oscillations are only found for large η as strong gyrotaxis is required to draw cells horizontally both into and away from the descending structures. However, they may not be observed experimentally as the time scale for overstability may be larger than for nonlinear effects to dominate.

6.2.3. *Model C, case II: the existence of non-hydrodynamic modes*

In this section, stability is explored when the two phototaxis parameters, ζ and χ, are varied for $d = 20$, $\kappa = 1.2$ and $d^2\eta = 4$. Figure 15 shows the associated neutral curves as the phototaxis strength parameter ζ is varied when $\chi = 2$ (where $I_s > I_c$). As ζ increases from $\zeta = 0$ to $\zeta = 4$, the trend in the stability curves is similar to that seen for increasing χ between $0 < \chi < 1$ in models A and B, where increasing ζ destabilizes the system and the critical wavenumber becomes zero, $k_c = 0$.

Interestingly, this trend continues as ζ increases further, and for approximately $\zeta > 5$ the Rayleigh number for small wavenumbers crosses the axis $R = 0$ in a smooth fashion. Physically, setting $R = 0$ uncouples the cell dynamics from the Navier–Stokes equations. This implies that under conditions of zero flow, $U = 0$, a destabilizing mechanism still exists. These non-hydrodynamic modes arise due to self-shading within the suspension (see figure 16). The mechanism for the instability is as follows. After perturbation, cells in the less concentrated regions receive too much light, due to decreased shading, and swim sideways into the densely concentrated regions to avoid the light. Thus, the perturbation may grow, tempered by diffusion, leading to instability. These modes are only possible because the torque due to ∇I means that cells can on average swim horizontally. These non-hydrodynamic modes do not exist in models A, B or C(I), and were not found in any of the gravitaxis, gyrotaxis
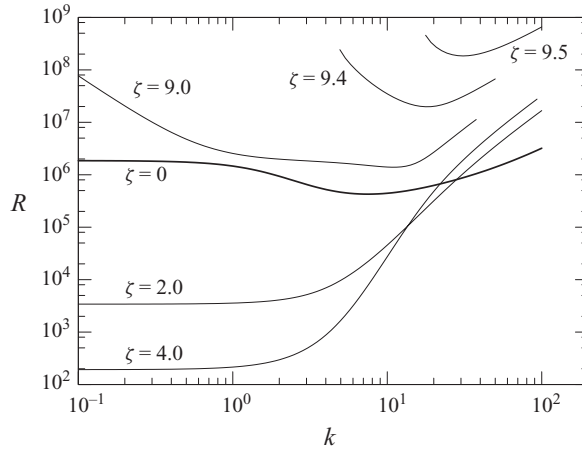
FIGURE 15. Curves of neutral stability for model C, case II, where $d = 20$, $\kappa = 1.2$, $\chi = 2.0$, $d^2\eta = 4$ and ζ varies.
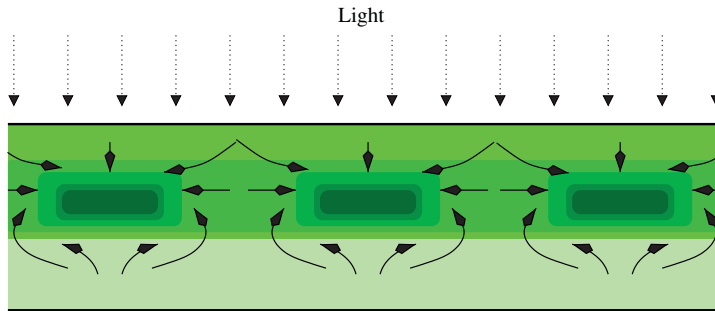

FIGURE 16. (Colour online available at journals.cambridge.org/FLM) An illustration of how non-hydrodynamic modes can arise due to self-shading for model C, case II. The arrows indicate the trajectories of swimming cells that are subject to a gravitational torque as well as an effective phototactic torque that biases their swimming direction up illumination gradients in weak light and down gradients in bright light. Cells in the less concentrated regions receive too much light and, on average, swim with a horizontal component towards more concentrated zones. Notably, for this model alone, mean horizontal swimming can occur without viscous torques associated with fluid flow. Such instabilities can develop for the steady states presented in figure 5 for an intermediate range of ζ.

or phototaxis models of Childress *et al.* (1975), Bees & Hill (1998) and Vincent & Hill (1996). In those models, cells are restricted to swimming purely upwards or downwards on average when $U = 0$; there is no mechanism for horizontal movement without fluid flow.

Figure 17 shows growth rate curves for the non-hydrodynamic version of case II, where $U = 0$. The existence of an instability mechanism in the absence of fluid flow is confirmed by the presence of positive growth rates, $\sigma > 0$, for small k when $5 < \zeta < 9.25$ (and solutions persist when the number of nodes is increased). Interestingly, when $\zeta > 9.25$ the growth rates are negative once again. This is because for large ζ the equilibria are distributed more uniformly, as discussed in §6.1, so perturbations have less effect on shading. For all parameter values investigated, no oscillatory modes were found for model C, case II.
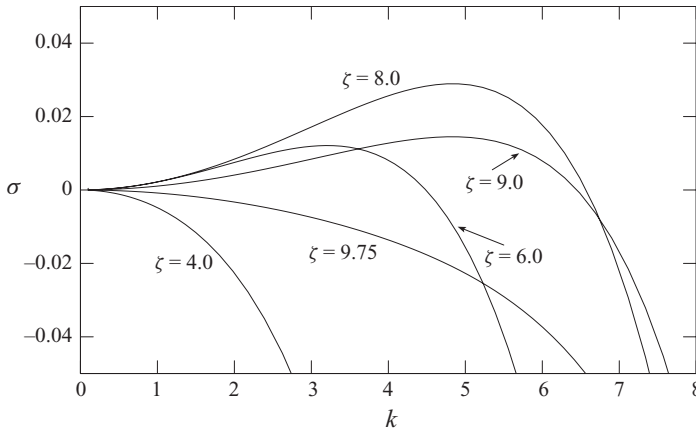
FIGURE 17. Growth rate curves for model C, case II, for no fluid flow ($U = R = 0$, $d = 20$), $\kappa = 1.2$, $\chi = 2.0$, $d^2\eta = 4$, and ζ varies. As ζ increases beyond $\zeta = 4.0$ some growth rates become positive, but when $\zeta = 9.75$ the growth rates are negative for all k.

In figure 15, hydrodynamic modes (with one convection cell) are also shown for $\zeta \geqslant 9$. The almost uniform concentration profile at equilibrium shown in figure 5 indicates that gyrotaxis is the dominant mechanism responsible for these hydrodynamic modes, since the gyrotactic instability is independent of the vertical density gradient. The suspension is stabilized and the non-zero critical wavenumber k_c increases as ζ increases from $\zeta = 9$. It is unclear where these neutral curves grow from, since hydrodynamic curves for $\zeta < 9$ are very difficult to trace numerically as they are entangled with non-hydrodynamic modes. It is also unclear whether the hydrodynamic or the non-hydrodynamic modes will be observed; which mode one is likely to see will depend on growth rates. Of course, in reality any aggregations of a finite size such as the non-hydrodynamic modes will initiate fluid motions, so that an instability may be initiated non-hydrodynamically but is likely to drive fluid motion shortly after. If $\zeta > 9$ (approximately), figure 17 demonstrates that the non-hydrodynamic modes are stabilized for all wavenumbers and, therefore, in these cases the hydrodynamic modes shown in figure 15 are the most unstable modes of instability. The trend in $\zeta > 9.0$ is similar to that for increasing $\chi > 1$ in models A and B, in which all wavenumbers are stabilized and k_c increases with χ.

Figure 18 explores the effects of varying the phototaxis torque strength when $\chi = 0.5$ (i.e. $I_s < I_c$, meaning that none of the cells have enough light). For all values of ζ, the peak of the equilibrium profile is at the top of the layer, $z = 0$. The maximum concentration increases with ζ due to an increase in the phototactic response. The neutral curves in figure 18 indicate that this significantly stabilizes wavenumbers $k \leqslant 60$ (due to increased effects of fluid damping at the upper boundary), and that both the critical wavenumber and the stability increase with increasing ζ. Varying $0 < \zeta < 4$ and $\chi > 0$ provides behaviour qualitatively similar to that of case I.

7. Conclusions

In this paper, we have presented three novel approaches to amalgamate the effects of phototaxis and gyrotaxis in a rationally based description of bioconvection, within the framework proposed by Pedley & Kessler (1990). This is the first such description of these two important behavioural traits and their impact on pattern formation in
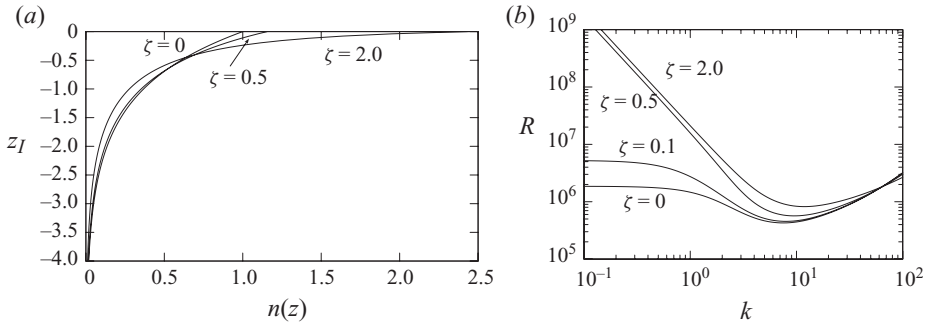
FIGURE 18. Concentration profiles (*a*) and corresponding neutral curves (*b*) for model C (II), where $d = 20$, $\kappa = 1.2$, $\chi = 0.5$, $d^2\eta = 4$ and ζ varies. For clarity, only $-4 \leqslant z \leqslant 0$ is shown.

suspensions of cells. Whilst the investigation of bioconvection is justified in its own right, the recent interest in the culture of algae for biofuel production underlines the importance of studying biased swimming microorganisms in layers (as here) and their transport properties in tubes (Bees & Croze 2010). To help improve the economic viability of biofuels, one should look for methods to reduce the energy input into such systems. Photo-gyrotactic behaviour may allow efficient mixing and concentration of the algae via several routes: photo-gyrotactic focusing to self-concentrate the cells, photo-gyrotactic focusing to prevent cells interacting with vertical boundaries where they might foul the surface, mixing of nutrients through bioconvective circulation, a bioconvective 'Cheese-plant effect' to allow greater light penetration into deep concentrated suspensions (Bees & Croze 2010), or even the effective use of light to block bioconvection patterns, if so desired.

The three models modify three distinct aspects of the swimming behaviour of the cells. In model A, the swimming speed is set to be a function of light intensity. In model B, each cell responds to light by adjusting its centre-of-mass offset (the distance between the centre-of-mass and centre-of-buoyancy) or, to the same end, the sedimentary torque (due to the asymmetric arrangement of body and anterior flagella) by modulating its symmetric flagellar beat. Model C introduces a new reactive torque due to phototaxis, induced via an asymmetric flagellar beat pattern. Model C was refined into two aspects: case I explored the torque relative to the axes of the incident light and case II investigated effects due the gradient of light intensity associated with shading by the cells. In all models, the momentum equation was coupled to a cell conservation equation via a negative buoyancy term due to the presence of the cells (for simplicity, we choose the simplest description). Furthermore, swimming cell flux is a function of fluid velocity, determined by solutions of a Fokker–Planck description for the orientation distribution of the cells. Light intensity was modelled using the Beer–Lambert law.

Linear analyses were performed to assess the linear stability of equilibrium profiles. For model A, the solution to the Fokker–Planck equation could be quoted from the literature. However, for models B and C, additional solutions were required. Asymptotic and numerical methods were adopted to explore the solution behaviour: in all cases, excellent agreement was found between solutions from the asymptotic and numerical methods, providing confidence in the results.

To be specific, the alga *C. augustae* was investigated in detail, although the models presented here are applicable to a wide range of microorganisms. The parameters for the magnitude of phototaxis, χ and ζ, and gyrotaxis, η, were of significant

interest. In all three models, for sufficiently large values of χ (or ζ in model CII), the maximum of the concentration profile at equilibrium was located below $z = 0$, creating a gravitationally stable region overlying an unstable region. For models A–C (case I), similar stability results were found for a wide range of parameter values: for all values of η, sufficiently large χ stabilized all wavenumbers and resulted in a non-zero critical wavenumber. Penetrative bioconvection, where fluid motions from the unstable region penetrated into the stable region, causing the whole fluid layer to become unstable, occurred unless the stable layer was so large that a mode-two solution was preferred. When gyrotaxis was sufficiently strong (large η), two different instability mechanisms were found and discussed. The overstability for small χ arose due to gyrotactic cells in the shear flow at the rigid upper boundary re-orientating to swim away from the downwelling fluid (as also observed by Hill *et al.* 1989 in a deterministic model of gyrotactic cells). The overstability for large χ was due to a combination of self-shading and gyrotaxis within the bulk of the suspension, which caused the cells near the light source to swim away from the downwelling fluid. In one respect, gyrotaxis and phototaxis act in opposite ways, since sufficiently large gyrotaxis destabilizes the system compared to the case $\eta = 0$, but sufficiently large phototaxis stabilizes the system for any η.

The above agreement between the models is noteworthy considering the different roots of the photo-gyrotactic mechanism. For the stability analysis, the main difference between models A and B is the formulation of the diffusion tensor, which is dependent on light intensity in model B and not in model A. The linear equations for model C, case I, are also similar except with different functional forms. The effects of illumination in other orientations in model C, such as from the side, have not been considered here, but are an obvious avenue of future research.

However, it is interesting to observe that model C (case II), in which cells react to local gradients in light intensity, produced radically different stability results: non-hydrodynamic modes arose due to self-shading of cells within the suspension. Such unstable solutions have not been found previously for phototactic, gravitactic or gyrotactic systems. However, non-hydrodynamic modes are unlikely to be observed experimentally as nonlinear effects would probably give rise to gyrotaxis and fluid flow. Perhaps a system with cells in agar would provide evidence for such an instability.

The validity of the models should, of course, be questioned. Model A was formulated such that cells react to a bright light by swimming backwards, an effect that is not seen in laboratory cultures of *C. augustae* (although cells can swim backwards during a photophobic response, Hegemann & Bruck 1989). It is known that cells phototactically adjust their swimming stroke (Rüffer & Nultsch 1991). Swimming backwards aside, swimming speed control is likely to be one component of the measurable phototactic response. The precise form of the functional response is yet to be determined experimentally (but is unlikely to be a simple linear function as assumed herein). Furthermore, the idealization in model A of a diffusivity that is independent of light intensity should be addressed. We chose this reduction, in the absence of any experimental data, as the obvious alternatives of a linear or quadratic dependence on the difference between light intensity and the critical value lead invariably to non-physical or singular solutions. In model B, the cells act as though their centre-of-mass varies with light intensity. This is perhaps only likely over a much longer time frame than the bioconvection experiments; starch deposits in the chloroplast (thought responsible for bottom-heaviness in *C. augustae*) can vary greatly in response to environmental stress (Zhang, Happe & Melis 2002). However, the complementary mechanism of sedimentary torque due to drag on the flagella may

vary over much smaller time scales. The phototactic torque in model C potentially may be determined by observing changes in flagella beat pattern in response to illumination (Rüffer & Nultsch 1991). The model is consistent with the observation of Häder (1987) for *Euglena gracilis* cells: when light is sufficiently bright, negative phototaxis dominates negative gravitaxis, and the cells swim downwards. However, by tracking cells, Hill & Häder (1997) inferred that phototaxis in *C. augustae* does not quite act as though there was a simple torque; the response is better approximated by a linear rather than sinusoidal curve. Model C is thus a first attempt at constructing a simple model for a complex set of processes. It is likely that all three models (and the two cases in model C) play some role in the photo-gyrotactic response of swimming cells. However, it should be noted that parameters, such as the critical light intensity, do not necessarily take the same value across all three models. Therefore, one may observe a cascade of photo-gyrotactic behaviour.

One significant assumption in the models is that all cells are effectively the same, exhibiting the same swimming speed in the dark and critical light intensity I_c. Experimental evidence for populations of cells (Hill & Häder 1997; Vladimirov *et al.* 2004) demonstrates that this is not the case, suggesting that the cascade referred to above may be somewhat smeared out. A more realistic model should incorporate this aspect (as in Bees & Hill 1998, for cell swimming speed V_n). For a more accurate expression of the diffusion tensor $\boldsymbol{D}$, generalized Taylor dispersion theory for the gyrotaxis-only case (Hill & Bees 2002; Manela & Frankel 2003), could be amended for photo-gyrotaxis. However, the Fokker–Planck equation and the general Taylor dispersion theory give similar results for small flows (Hill & Bees 2002).

In Williams & Bees (2011), the effects of illumination on bioconvective patterns, particularly the wavelength of the initial instability, were explored. These results can be compared directly with the theoretical predictions for hydrodynamic modes presented here. However, note that the initial wavenumber, for a growing mode at a Rayleigh number above the critical value, and the critical wavenumber, at the critical Rayleigh number with neutral stability, are closely related but not the same thing. Table 7 presents a selection of the experimental results and predictions from models A and B (Williams & Bees 2011 compare experiments and theory in more detail). The suspension was mixed with an offset rotating bed and then the emerging pattern was recorded and Fourier-analysed. Each experimental run was repeated up to eight times with the same cells to obtain the mean data presented, and each full experimental was repeated up to three times with different cells to check for repeatability. The experimental initial wavelength was first found to decrease followed by an increase as I was increased from zero. This qualitative behaviour was matched by theoretical predictions as χ was increased from zero, and the wavenumbers were mostly of a similar size. However, the critical wavenumbers predicted by the theory were up to five times larger than the experimental initial wavenumbers for zero and large illumination, in line with the gyrotaxis-only case (Bees & Hill 1997, 1998). For intermediate illumination, the theoretical wavenumbers were slightly smaller than those observed in experiments. (Note that $k_0 = 9.6$ corresponds to a dimensional wavelength of 0.2 cm.) We do not know accurately the value of some of the parameter values, particularly those associated with phototaxis, so one could attempt to fit the data to obtain better agreement. This, however, is not our purpose; instead we look to investigate qualitative features and mechanisms, and incorporate improved experimental measurements of the parameters from independent experiments when they become available.

There are other reasons why there might be a discrepancy between theory and experiments. Firstly, it is difficult to prescribe the experimental parameters such that

Experimental results

Illumination	d	I (lux)	k_0	R
Red	34.6	Any/0	10.12	2.18×10^6
White	34.6	645	8.23	2.18×10^6
White	34.6	1330	7.55	2.18×10^6
White	34.6	2020	8.45	2.18×10^6
White	34.6	2710	9.64	2.18×10^6
White	34.6	3390	10.24	2.18×10^6
White	34.6	4080	11.34	2.18×10^6
White	34.6	4780	12.23	2.18×10^6

Theoretical predictions

d	χ	k_c (A)	k_c (B)	R_c (A)	R_c (B)
34.6	0	45.3	45.3	2.77×10^6	2.77×10^6
34.6	0.6	12.5	5.04	1.32×10^6	7.17×10^5
34.6	1.0	5.57	4.45	4.02×10^5	3.17×10^5
34.6	1.2	5.57	4.21	2.71×10^5	2.36×10^5
34.6	1.4	18.1	14.1	1.09×10^7	1.16×10^7
34.6	1.45	37.1	30.9	3.63×10^7	3.95×10^7
34.6	1.5	62.0	51.8	9.16×10^7	1.01×10^8

TABLE 7. Summary of experimental results for a cell concentration of 5.05×10^6 cells cm^{-3} and depth $H = 0.306$ cm (giving $d = 34.6$), illuminated from above with either red or white light, where wavenumbers are the mean of eight experimental runs performed with the same cells; and corresponding theoretical predictions for models A and B. Here, $\kappa = 20.3$, $d^2 \eta = 16$, $\lambda = 2.2$ and $\tau = 5$ s. Cells do not respond phototactically to red light. Wavenumbers are non-dimensional.

we are close to the neutral stability curve; the further that we are in parameter space from the minimum of the neutral curve the less likely it is that the minimum will predict the correct wavenumber. Secondly, in experiments it may be difficult to identify the initial instability before nonlinearities play a role. Finally, there are two issues associated with time scales: have the effects of mixing sufficiently diminished, and has the equilibrium distribution had sufficient time to form before the onset of pattern formation? In the experimental protocol employed by Williams & Bees (2011), the effects of mixing were minimized by a novel automated method. Whatever the experimental mixing methodology, it is clear that there is likely to be some vanishingly small effect of the mixing on the initial perturbation; fluid motions inevitably remain and contribute to the onset of pattern formation. To establish whether the bulk of the flow has diminished, we use an argument similar to Hill *et al.* (1989) and assume that the Petri dish is in solid-body rotation with angular velocity $\boldsymbol{\Omega}$ until the mixing stops and the container instantaneously comes to rest. The time for spindown is $O(E^{-1/2}|\boldsymbol{\Omega}|^{-1})$, where $E = \nu/\boldsymbol{\Omega} H^2$ is the Ekman number (ν is the viscosity and H is the layer depth). The speed of the mixer in Williams & Bees (2011) provides $|\boldsymbol{\Omega}| = 21$ s^{-1}. Hence, for a shallow layer ($H = 0.31$ cm), $E = 5.1 \times 10^{-3}$ and the residual fluid motion decays in 0.69 s. Since the patterns occur after several tens of seconds, we conclude that the flow was likely to have mostly diminished before pattern formation began. For the formation of the equilibrium solution, if the average cell-swimming speed is 63 μm s^{-1} (Hill & Häder 1997), and non-advected cells swim upwards at an average of 56 % of this speed (calculated from Bees, Hill & Pedley 1998), then an average cell would take 85 s to swim the layer depth, H. This suggests that the

cells may not have sufficient time to form the equilibrium distributions before pattern onset. However, the equilibrium profile will certainly have been approached.

The three combined photo-gyrotactic models presented here represent a significant advance in constructing realistic and rational models of bioconvection under illumination. It is likely that gyrotactic microorganisms use a combination of the three mechanisms explored here to photo-orientate. These models could be used as a foundation upon which studies of pattern formation could be conducted under various conditions for a diverse range of microorganisms.

Supplementary data are available at journals.cambridge.org/flm.

Appendix A. Definitions of a, $\tilde{a}$ and $\bar{a}$

Here a, $\tilde{a}$ and $\bar{a}$ are defined as

$$a_{n,m} = -\frac{m+2}{(m+1)(2m+3)}a_{n-1,m+1} + \frac{m-1}{(2m-1)m}a_{n-1,m-1} + \frac{b_{n,m}}{m(m+1)},$$

where

$$b_{n+1,m} = \begin{cases} 0, & \forall \quad n+m \text{ even}, \\ \dfrac{(2m+1)\Gamma\dfrac{n+1}{2}\Gamma\dfrac{n+2}{2}}{4\Gamma(n+1)\Gamma\dfrac{n-m+3}{2}\Gamma\dfrac{n+m+4}{2}}, & \forall \quad n+m \text{ odd}, \end{cases} \tag{A 1}$$

$$\tilde{a}_{n,m} = -\frac{m+2}{(m+1)(2m+3)}\tilde{a}_{n-1,m+1} + \frac{m-1}{(2m-1)m}\tilde{a}_{n-1,m-1} + \frac{\tilde{b}_{n,m}}{m(m+1)},$$

where

$$\tilde{b}_{n+1,m} = \begin{cases} 0, & \forall \quad n+m \text{ even}, \\ -\dfrac{(2m+1)\Gamma\dfrac{n+1}{2}\Gamma\dfrac{n+2}{2}(n^2+5n+4+m+m^2)}{16\Gamma(n+1)\Gamma\dfrac{n-m+5}{2}\Gamma\dfrac{n+m+6}{2}}, & \forall \quad n+m \text{ odd}, \end{cases} \tag{A 2}$$

$$\bar{a}_{n,m} = -\frac{m+3}{(m+1)(2m+3)}\bar{a}_{n-1,m+1} + \frac{m-2}{(2m-1)m}\bar{a}_{n-1,m-1} + \frac{\bar{b}_{n,m}}{m(m+1)},$$

where

$$\bar{b}_{n+1,m} = \begin{cases} 0, & \forall \quad n+m \text{ even}, \\ -\dfrac{(2m+1)\Gamma\dfrac{n+2}{2}\Gamma\dfrac{n+3}{2}(n+4)}{8\Gamma(n+2)\Gamma\dfrac{n-m+5}{2}\Gamma\dfrac{n+m+6}{2}}, & \forall \quad n+m \text{ odd}. \end{cases} \tag{A 3}$$

Appendix B. Amendments to the solution of the Fokker–Planck equation: model C

B.1. *Model C, case I*

Here, we put $h(I) = 1$, as for case A. For model C, case I, we consider light from above, such that $\pi = k$, and we set $\beta_1 = 1$ and $\beta_2 = 0$. The Fokker–Planck equation becomes

$$(1 - \chi\zeta e^{\kappa m}(\chi e^{\kappa m} - 1))(\mathbf{k} \cdot \nabla_p f - 2(\mathbf{k} \cdot \mathbf{p})f) + \eta\omega \cdot (\mathbf{p} \wedge \nabla_p f)$$
$$+ 2\eta\alpha_0[\mathbf{p} \cdot \mathbf{e} \cdot \nabla_p f - 3\mathbf{p} \cdot \mathbf{e} \cdot \mathbf{p} f] = \lambda^{-1}\nabla_p^2 f, \quad \text{(B 1)}$$

where

$$\zeta = 4f_m/h_n mg \quad \text{(B 2)}$$

is a new parameter only present in model C and is a measure of the strength of the torque due to phototaxis. In this case, $\bar{\mathbf{k}}(I) = (1 - \chi\zeta e^{\kappa m}(\chi e^{\kappa m} - 1))\mathbf{k}$ in (3.18).

For the no-flow steady state, we again obtain (4.2) with, in this case,

$$\Lambda(z) = \lambda\left(1 - \zeta\chi e^{\kappa m^0(z)}\left(\chi e^{\kappa m^0(z)} - 1\right)\right). \quad \text{(B 3)}$$

With this definition of $\Lambda(z)$, the solution is given by (4.3). At first order in ϵ, (B 1) yields an equation similar to that for model A (4.6), but with $\Lambda(z)$ redefined, and an extra term on the right-hand side:

$$-\lambda\zeta\chi\kappa\mu_\lambda m^1 e^{\kappa m^0}\left(2\chi e^{\kappa m^0} - 1\right)e^{\Lambda\cos\theta}(\Lambda\sin^2\theta - 2\cos\theta). \quad \text{(B 4)}$$

As for model B, the solution excluding this last term is given by (4.7) and (4.8), but with $\Lambda(z)$ replacing λ. For the new term representing a phototactic torque, substitute

$$f^1 = \lambda\zeta\chi\kappa\mu_\Lambda m^1 e^{\kappa m^0}\left(2\chi e^{\kappa m^0} - 1\right)\mathscr{H}(\theta, z), \quad \text{(B 5)}$$

into the equation, with $x = \cos\theta$, to give $\mathscr{H}(x, z) = e^{\Lambda x}(K_1(\Lambda(z)) - x)$. Contributions to $\langle \mathbf{p} \rangle$ and $\mathbf{D}$ are calculated from (3.7) and (3.8) and shown in table 3.

B.2. *Model C, case II*

Consider the case where cells respond to local gradients in light intensity (see (2.4); $\beta_1 = 0$ and $\beta_2 = 1$). Equation (3.18) results with $h(I) = 1$ and

$$\bar{\mathbf{k}}(I) = \mathbf{k} - c\nabla I, \quad \text{where} \quad c = \zeta\chi I(\chi I - 1). \quad \text{(B 6)}$$

Since $\bar{\mathbf{k}}(I)$ can be treated as a constant in orientation space, one obtains (4.1) with $\mathbf{k}$ replaced by $\bar{\mathbf{k}}$.

Since $I = e^{\kappa(m^0 + \epsilon m^1)} = e^{\kappa m^0} + \epsilon\kappa m^1 e^{\kappa m^0} + O(\epsilon^2)$, expand c and $\bar{\mathbf{k}}$ in ϵ to yield

$$\bar{\mathbf{k}} = (1 - C^0)\mathbf{k} - \epsilon C^1\mathbf{k} - \epsilon c^0 \mathbf{G}^1, \quad \text{(B 7)}$$

where $\mathbf{G}^1 = \nabla_H m^1$, $\nabla_H = (\partial/\partial x, \partial/\partial y, 0)^T$,

$$c^0 = \zeta\chi\kappa e^{2\kappa m^0}(\chi e^{\kappa m^0} - 1), \quad C^0 = c^0\frac{dm^0}{dz},$$

$$C^1 = \zeta\chi\kappa e^{2\kappa m^0}\left(\kappa n^0\left(3\chi e^{\kappa m^0} - 2\right)m^1 + \left(\chi e^{\kappa m^0} - 1\right)\frac{dm^1}{dz}\right). \quad \text{(B 8)}$$

At zeroth order in ϵ, we again obtain (4.2) with, in this case, $\Lambda(z) = \lambda(1 - C^0(z))$. The solution is given by (4.3), with the new $\Lambda(z)$.

For weak ambient flow, at order ϵ, one obtains an equation similar to that for model A (4.6), but with $\Lambda(z)$ redefined, and an extra term on the right-hand side:

$$-\lambda C^1 \left(\mathbf{k} \cdot \hat{\boldsymbol{\theta}} \frac{\partial f^0}{\partial \theta} - 2 \cos \theta f^0 \right) - \lambda c^0 \left(\mathbf{G}^1 \cdot \hat{\boldsymbol{\theta}} \frac{\partial f^0}{\partial \theta} - 2 \mathbf{G}^1 \cdot \mathbf{p} f^0 \right). \tag{B 9}$$

This equation is solved by considering each term on the right-hand side separately. For the first group in (B 9), consider a solution of the form $f^{1(1)} = \lambda C^1 \mu_\Lambda \mathcal{H}_1(\theta)$. With $x = \cos \theta$, this provides $((1-x^2)\mathcal{H}_1')' - \Lambda((1-x^2)\mathcal{H}_1)' = -[e^{\Lambda x}(1-x^2)]'$. This is of the same form as (4.13) in model B, hence $\mathcal{H}_1(x, z)$ is given in (4.14) and the contributions to $\langle \mathbf{p} \rangle$ and $\mathbf{D}$ are the same as in model B but with a different $\Lambda(z)$ (see table 3).

For the penultimate term in (B 9), put $f^{1(2)} = -\mu_\Lambda \lambda c^0 (G_1^1 \cos \phi + G_2^1 \sin \phi) \mathcal{H}_2(\theta)$:

$$((1-x^2)\mathcal{H}_2')' - \frac{\mathcal{H}_2}{(1-x^2)} - \Lambda((1-x^2)\mathcal{H}_2)' = -x\Lambda(1-x^2)^{1/2}e^{\Lambda x}. \tag{B 10}$$

Equation (B 10) can be solved by expanding asymptotically with Λ and associated Legendre polynomials (an approach successfully employed in Pedley & Kessler 1990) to give $h_2(x) = \sum_{n=1}^{\infty} \Lambda^n H_n(x)$, and $H_n(x) = \sum_{r=1}^{n+1} \hat{a}_{n,r} P_r^1(x)$, where $\hat{a}_{n,r} = 0$ for $n + 1 < r$ or $n, r < 1$. Hence,

$$\hat{a}_{n,m} = -\frac{m+2}{(m+1)(2m+3)} a_{n-1,m+1} + \frac{m-1}{(2m-1)m} a_{n-1,m-1} + \frac{\hat{b}_{n,m}}{m(m+1)}, \tag{B 11}$$

where

$$\hat{b}_{n,m} = \frac{(2m+1)n}{2(n!)m(m+1)} \int_{-1}^{1} (1-x^2)^{1/2} x^n P_m^1(x) \, \mathrm{d}x = nb_{n+1,m}, \tag{B 12}$$

with $b_{n+1,m}$ defined in (A 1), and $n + 2 \geqslant m$. Since $b_{n+1,m} = 0$ if $n + m$ is even, $\hat{a}_{n,m} = 0$ for $n + m$ even. Contributions to the mean cell-swimming direction, $\langle \mathbf{p} \rangle$, and diffusion tensor, $\mathbf{D}$, are calculated from (3.7) and (3.8) and presented in table 3.

The final term on the right-hand side in (B 9) has a similar form. Put $f^{1(3)} = -2(\mu_\Lambda \lambda c^0/\Lambda)(G_1^1 \cos \phi + G_2^1 \sin \phi) \mathcal{H}_3(\theta)$. The contributions to the mean cell-swimming direction and diffusion tensor are stated in table 3.

Appendix C. Derivation of equations for linear-stability analysis for models B and C

C.1. *Model B*

For model B, we set $V_s(I) = 1$, and so

$$\frac{\partial n^1}{\partial t} = -\partial_3 n^0 u_3^1 - \frac{d\bar{K}_2}{\bar{K}_1} \partial_3 n^0 \langle p \rangle_3^1 - \frac{d\bar{K}_2}{\bar{K}_1} n^0 \partial_i \langle p \rangle_i^1 - \frac{d\bar{K}_2}{\bar{K}_1} \partial_i n^1 \langle p \rangle_i^0$$
$$- \frac{d\bar{K}_2}{\bar{K}_1} n^1 \partial_i \langle p \rangle_i^0 + D_{ij}^0 \partial_i \partial_j n^1 + \partial_i D_{ij}^0 \partial_j n^1 + D_{33} \partial_i \partial_j n^0 + \partial_i D_{i3}^1 \partial_3 n^0. \tag{C 1}$$

Expanding $\partial_i \langle p \rangle_i^1$ and $\partial_i D_{i3}^1$, employing the additional terms from (4.15), and substituting (5.11), yields

$$\left\{ P_V(z) \frac{\mathrm{d}^2}{\mathrm{d}z^2} - \frac{d\bar{K}_2}{\bar{K}_1} K_1(z) \frac{\mathrm{d}}{\mathrm{d}z} - P_H(z)k^2 - \sigma - \frac{d\bar{K}_2}{\bar{K}_1} \frac{\mathrm{d}K_1}{\mathrm{d}z} + \frac{\mathrm{d}P_V(z)}{\mathrm{d}z} \frac{\mathrm{d}}{\mathrm{d}z} \right.$$
$$\left. + \lambda \chi \kappa e^{\kappa m^0} P_R(z; d) \right\} \Phi + \lambda \chi \kappa e^{\kappa m^0} P_M(z; d) M(z)$$
$$= \left\{ \frac{\mathrm{d}n^0}{\mathrm{d}z} - \eta P_5(z; d) \frac{\mathrm{d}^2}{\mathrm{d}z^2} - \eta P_6(z; d) \frac{\mathrm{d}}{\mathrm{d}z} + \eta P_7(z; d)k^2 \right\} U(z), \tag{C 2}$$

where

$$
\left.\begin{aligned}
P_R(z;d) &= -\frac{d\bar{K}_2}{\bar{K}_1}n^0 K_6(z) + \frac{dn^0}{dz}(K_8(z) - 2K_1(z)K_6(z)), \\
P_M(z;d) &= -\frac{d\bar{K}_2}{\bar{K}_1}\left[\frac{dn^0}{dz} + n^0\left(\kappa\frac{dm^0}{dz} + \frac{d}{dz}\right)\right]K_6(z) + \frac{d^2 n^0}{dz^2}(K_8(z) \\
&\quad - 2K_1(z)K_6(z)) + \frac{dn^0}{dz}\left[\kappa\frac{dm^0}{dz} + \frac{d}{dz}\right](K_8(z) - 2K_1(z)K_6(z)), \\
P_5(z;d) &= \frac{dn^0}{dz}A_1(z) + \frac{d\bar{K}_2}{\bar{K}_1}n^0 A_2(z), \quad P_7(z;d) = \frac{dn^0}{dz}A_5(z) - \frac{d\bar{K}_2}{\bar{K}_1}n^0 A_6(z), \\
P_6(z;d) &= \frac{d\bar{K}_2}{\bar{K}_1}\frac{dn^0}{dz}A_3(z) - \frac{d^2 n^0}{dz^2}A_4(z) + \frac{d\bar{K}_2}{\bar{K}_1}n^0\frac{dK_4(z)}{dz} \\
&\quad - \frac{dn^0}{dz}\frac{d(K_5(z) - 2K_1(z)K_4(z))}{dz},
\end{aligned}\right\} \tag{C3}
$$

with $n^0 = n^0(z)$ and $m^0 = m^0(z)$ and Λ and K_i are all functions of z, whereas $\bar{K}_1$ and $\bar{K}_2$ are constants. Here $A_i(z)$, $P_V(z)$ and $P_H(z)$ are as in table 4, but now depend on $\Lambda(z)$ defined in table 3.

Equations (C2) and (5.17) are similar: the right-hand sides of both equations look the same, although the definitions for $P_5(z;d)$, $P_6(z;d)$ and $P_7(z;d)$ are different; the non-constant K_i lead to extra terms on the left-hand side with derivatives of $K_i(z)$; and $P_M(z;d)$ and $P_R(z;d)$ differ. Again, setting $\chi = 0$ gives the linear-stability equation of Bees & Hill (1998) for the gyrotaxis-only case.

Boundary conditions are as in model A except for the no-flux conditions, which become

$$
\left.\begin{aligned}
&\frac{d\bar{K}_2}{\bar{K}_1}K_1\Phi - K_2\frac{d\Phi}{dz} = 0 \quad \text{on} \quad z = 0, \quad \frac{d\bar{K}_2}{\bar{K}_1}K_1\Phi - K_2\frac{d\Phi}{dz} \\
&+ \lambda\chi\kappa e^{\kappa m^0}\left(d\frac{\bar{K}_2}{\bar{K}_1}K_6 n^0 - \frac{dn^0}{dz}(K_8 - 2K_1 K_6)\right)M = 0 \quad \text{on} \quad z = -1.
\end{aligned}\right\} \tag{C4}
$$

Note that in some situations Λ may be close to zero. This may cause problems when solving the equations numerically, as many functions appear to involve division by Λ. However, Taylor-expanding each K_i and J_i reveals that they are finite and converge as Λ tends to zero. Such expressions are used in the numerical programme to eliminate such issues when Λ is small.

C.2. *Model C, case I*

For model C, case I, we also set $V_s(I) = 1$ and obtain the cell conservation equation to order ϵ as (C1) from the model B analysis, but with different expressions for $\partial_i\langle\boldsymbol{p}\rangle_i^1$ and $\partial_i\boldsymbol{D}_{i3}^1$: derived from (4.7) and (4.8) plus the extra terms due to phototaxis in table 3. Hence, substituting (5.11) gives

$$
\begin{aligned}
&\left\{P_V(z)\frac{d^2}{dz^2} - \frac{d\bar{K}_2}{\bar{K}_1}K_1(z)\frac{d}{dz} - P_H(z)k^2 - \sigma - \frac{d\bar{K}_2}{\bar{K}_1}\frac{dK_1}{dz} + \frac{dP_V(z)}{dz}\frac{d}{dz}\right. \\
&\left.+ \lambda\zeta\chi\kappa e^{\kappa m^0}P_R(z;d)\right\}\Phi + \lambda\zeta\chi\kappa e^{\kappa m^0}P_M(z;d)M(z) \\
&= \left\{\frac{dn^0}{dz} - \eta P_5(z;d)\frac{d^2}{dz^2} - \eta P_6(z;d)\frac{d}{dz} + \eta P_7(z;d)k^2\right\}U(z), \tag{C5}
\end{aligned}
$$

where

$$
\left.\begin{aligned}
P_R(z;d) &= -\frac{d\bar{K}_2}{\bar{K}_1}n^0 K_6(z)\left(2\chi e^{\kappa m^0}-1\right) + \frac{dn^0}{dz}(K_8(z) \\
&\quad - 2K_1(z)K_6(z))\left(2\chi e^{\kappa m^0}-1\right), \\
P_M(z;d) &= -\frac{d\bar{K}_2}{\bar{K}_1}\left[K_6(z)\frac{dn^0}{dz} + n^0\left(\kappa\frac{dm^0}{dz}K_6(z)\left(4\chi e^{\kappa m^0}-1\right)\right.\right. \\
&\quad \left.\left.+ \frac{dK_6(z)}{dz}(2\chi e^{\kappa m^0}-1)\right)\right] + \frac{d^2n^0}{dz^2}(K_8(z)-2K_1(z)K_6(z)) \\
&\quad + \frac{dn^0}{dz}\left[\kappa\frac{dm^0}{dz}(K_8(z)-2K_1(z)K_6(z))\right. \\
&\quad \left.\times\left(4\chi e^{\kappa m^0}-1\right) + \frac{d(K_8(z)-2K_1(z)K_6(z))}{dz}(2\chi e^{\kappa m^0}-1)\right],
\end{aligned}\right\} \quad (C\,6)
$$

and $P_V(z)$, $P_H(z)$, $P_5(z;d)$, $P_6(z;d)$ and $P_7(z;d)$ are defined in table 4, and (C 3) except with the definition of Λ for model C, case I, in table 3. Here, $n^0 = n^0(z)$ and $m^0 = m^0(z)$. Equation (C 5) has the same form as (C 2) for model B but $P_M(z;d)$, $P_R(z;d)$ and $\Lambda(z)$ in $K_i(z)$ and $J_i(z)$ are different in each model (see table 3). The boundary conditions are the same as in model A except for the no-flux conditions which become the first line of (C 4), and on $z = -1$,

$$
\frac{d\bar{K}_2}{\bar{K}_1}K_1\Phi - K_2\frac{d\Phi}{dz} + \lambda\zeta\kappa e^{\kappa m^0}\left(2\chi e^{\kappa m^0}-1\right)\left(d\frac{\bar{K}_2}{\bar{K}_1}K_6 n^0 - \frac{dn^0}{dz}(K_8 - 2K_1 K_6)\right)M = 0. \tag{C\,7}
$$

C.3. *Model C, case II*

Following the same procedure as before yields

$$
\begin{aligned}
&\left\{P_V(z)\frac{d^2}{dz^2} - \frac{d\bar{K}_2}{\bar{K}_1}K_1(z)\frac{d}{dz} - P_H(z)k^2 - \sigma - \frac{d\bar{K}_2}{\bar{K}_1}\frac{dK_1}{dz} + \frac{dP_V(z)}{dz}\frac{d}{dz}\right. \\
&\quad \left. - P_R(z;d) - P_{R2}(z;d)\frac{d}{dz}\right\}\Phi - \left\{P_{M2}(z;d) - k^2 P_{M1}(z;d)\right\}M(z) \\
&= \left\{\frac{dn^0}{dz} - \eta P_5(z;d)\frac{d^2}{dz^2} - \eta P_6(z;d)\frac{d}{dz} + \eta P_7(z;d)k^2\right\}U(z),
\end{aligned} \tag{C\,8}
$$

where

$$
\begin{aligned}
P_R(z;d) &= \lambda\zeta\chi\kappa e^{2\kappa m^0}\left(\chi e^{\kappa m^0}-1\right)\left[\frac{d\bar{K}_2}{\bar{K}_1}\left(\frac{dn^0}{dz}K_6(z) + n^0\frac{dK_6(z)}{dz}\right)\right. \\
&\quad \left. - \frac{d^2n^0}{dz^2}(K_8(z)-2K_1(z)K_6(z)) - \frac{dn^0}{dz}\frac{d}{dz}(K_8(z)-2K_1(z)K_6(z))\right] \\
&\quad + 2\lambda\zeta\chi\kappa^2 n^0 e^{2\kappa m^0}\left(3\chi e^{\kappa m^0}-2\right)\left(\frac{d\bar{K}_2}{\bar{K}_1}K_6(z)n^0 - \frac{dn^0}{dz}(K_8(z)-2K_1(z)K_6(z))\right),
\end{aligned} \tag{C\,9}
$$

$$
P_{R2}(z;d) = \lambda\zeta\chi\kappa e^{2\kappa m^0}\left(\frac{d\bar{K}_2}{\bar{K}_1}K_6(z)n^0 - \frac{dn^0}{dz}(K_8(z)-2K_1(z)K_6(z))\right)(\chi e^{\kappa m^0}-1), \tag{C\,10}
$$

$$
\begin{aligned}
P_{M1}(z;d) &= \left[\frac{dn^0}{dz}\left(J_8(z) + \frac{2J_2(z)}{\lambda} - K_1(z)\left(J_7(z) + \frac{2J_1(z)}{\lambda}\right)\right)\right. \\
&\quad \left. - \frac{d\bar{K}_2}{\bar{K}_1}n^0\left(J_7(z) + \frac{2J_1(z)}{\lambda}\right)\right]\frac{C^0(z)}{(1-C^0(z))n^0},
\end{aligned} \tag{C\,11}
$$

$$P_{M2}(z;d) = \lambda \zeta \chi \kappa e^{2\kappa m^0} \kappa n^0 (3\chi e^{\kappa m^0} - 2) \left[\frac{d\bar{K}_2}{\bar{K}_1} \left(\frac{dn^0}{dz} K_6(z) + n^0 \frac{dK_6}{dz} \right) \right.$$

$$- \frac{d^2 n^0}{dz^2} (K_8(z) - 2K_1(z)K_6(z)) - \frac{dn^0}{dz} \frac{d}{dz} (K_8(z) - 2K_1(z)K_6(z)) \right]$$

$$+ \lambda \zeta \chi \kappa e^{2\kappa m^0} \left(\frac{d\bar{K}_2}{\bar{K}_1} K_6(z)n^0 - \frac{dn^0}{dz} (K_8(z) - 2K_1(z)K_6(z)) \right)$$

$$\times \left(\kappa \frac{dn^0}{dz} (3\chi e^{\kappa m^0} - 2) + 3\chi \kappa^2 (n^0)^2 e^{\kappa m^0} + 2\kappa^2 (n^0)^2 (3\chi e^{\kappa m^0} - 2) \right), \quad \text{(C 12)}$$

with $n^0 = n^0(z)$ and $m^0 = m^0(z)$. Here, $K_i(z)$ are functions of $\Lambda(z)$, as in table 2, and $C^0(z)$ and $C^1(z)$ are defined in (B 8). Note that $P_V(z)$ is defined in table 4, and $P_5(z;d)$, $P_6(z;d)$ and $P_7(z;d)$ are defined in (C 3). Equation (C 8) has a form similar to the linear-stability equation for model B (C 2), with new definitions for $P_R(z;d)$ and $P_{M2}(z;d)$. Also, (C 8) introduces another derivative of Φ multiplied by $P_{R2}(z;d)$, and a new term $P_{M1}(z;d)$ multiplied by k^2 due to derivatives in x and y from the gradient of I appearing in $\bar{k}(I)$ at order ϵ. The no-flux boundary conditions become

$$\frac{d\bar{K}_2}{\bar{K}_1} K_1 \Phi - K_2 \frac{d\Phi}{dz} + \lambda \zeta \chi \kappa e^{2\kappa m^0} (\chi e^{\kappa m^0} - 1) \frac{dM(z)}{dz}$$

$$\times \left(d\frac{\bar{K}_2}{\bar{K}_1} K_6 n^0 - \frac{dn^0}{dz}(K_8 - 2K_1 K_6) \right) = 0 \quad \text{on} \quad z = 0, \quad \text{(C 13)}$$

$$\frac{d\bar{K}_2}{\bar{K}_1} K_1 \Phi - K_2 \frac{d\Phi}{dz} + \lambda \zeta \chi \kappa e^{2\kappa m^0} \left[\kappa n^0 (3\chi e^{\kappa m^0} - 2)M(z) + (\chi e^{\kappa m^0} - 1) \frac{dM(z)}{dz} \right]$$

$$\times \left(d\frac{\bar{K}_2}{\bar{K}_1} K_6 n^0 - \frac{dn^0}{dz}(K_8 - 2K_1 K_6) \right) = 0 \quad \text{on} \quad z = -1. \quad \text{(C 14)}$$

Appendix D. Asymptotic analysis for a deep layer and weak illumination

Consider the case $\sigma = 0$, $k \sim 1$, $d^{-1} \ll 1$ and $\chi \ll 1$. If we write $\chi = \chi_{-1} d^{-1}$, where χ_{-1} is order one, then the analysis is similar to that of Bees & Hill (1998) up to third order, and so is only summarized here. Consider also that the gyrotaxis parameter is of the order d^n and P_V, P_H, P_5, P_6 and P_7 are constants, not dependent on z, assumed to be order one up to third order. This is valid as long as d is sufficiently large. Note that d is a ratio of the depth to the sublayer depth in the gyrotactic-only case. However, for the case of weak illumination, d is still a good approximation of this measure.

D.1. *Asymptotic analysis for model A*

D.1.1. *Asymptotic equilibrium solution*

Multiplying the equilibrium (5.1) by d^{-1} and writing $\chi = \chi_{-1} d^{-1}$ gives

$$d^{-1} m'' + (d^{-1} \chi_{-1} e^{\kappa m} - 1) m' = 0, \quad \text{(D 1)}$$

where primes indicate differentiation with respect to the dependent variable. The boundary conditions are $m = 0$ at $z = 0$ and $m = (e^{-d} - 1)/d$ at $z = -1$.

For the 'outer' solution, we expand m in powers of d^{-1}, so that $m = m_0 + d^{-1}m_{-1} + d^{-2}m_{-2} + \cdots$. Collecting powers of d^{-1}, it is easy to show that the solution is $m_{-1} = -1$ and $m_{-n} = 0$ for $n = 0, 2, 3, 4, \ldots$.

For the 'inner' solution, we scale $z_I = dz$ to magnify the top region of the fluid. Thus, $m'' + (d^{-1}\chi_{-1}e^{\kappa m} - 1)m' = 0$. We expand m in powers of d, as for the outer solution, whence $m_0 = A_0(e^{z_I} - 1)$ and the next order satisfies $m''_{-1} + \chi_{-1}e^{\kappa m_0}m'_0 - m'_{-1} = 0$. On matching the inner and outer solutions up to second order in the usual way (see Kevorkian & Cole 1981), we obtain $A_0 = 0$ and, hence, $m_{-1} = A_1(e^{z_I} - 1)$. The matching condition provides $A_1 = 1$, and at the next order

$$m''_{-2} - m'_{-2} + \chi_{-1}\,e^{\kappa m_0}m'_{-1} + \chi_{-1}\,e^{\kappa m_0}m'_0 = 0. \tag{D 2}$$

Hence, $m_{-2} = -\chi_{-1}z_I e^{z_I}$, where the constants of integration are found by applying the upper boundary condition and matching to the outer solution at third order.

D.1.2. *Asymptotic linear-stability analysis*

For the linear-stability analysis, terms from the equilibrium from §D.1.1 are now denoted by a superscript 0. Expanding for large d with $\sigma = 0$ and using the equilibrium solution, then (5.12) and (5.17) for the outer solution become

$$(D^2 - k^2)^2 U = -k^2 d^{-1}R\Phi, \tag{D 3}$$

$$\left(P_V D^2 - P_H k^2 - P_V d\left(1 - d^{-1}\chi_{-1}\left(1 - d^{-1}\kappa + \frac{d^{-2}\kappa^2}{2} - \dots\right)\right)D\right)\Phi = 0, \tag{D 4}$$

respectively. These equations have the same form as Bees & Hill (1998); the effects of non-zero χ do not come in until higher orders. The solutions are $\Phi = 0$ and

$$U = -kA(z + 1)\cosh k(z + 1) + (A + B(z + 1))\sinh k(z + 1), \tag{D 5}$$

where A and B are constants that can be expanded in terms of d^{-1}.

For the inner solution, we re-scale $z_I = dz$, such that (5.12) and (5.17) provide

$$\left(D_I^2 - d^{-2}k^2\right)^2 U = -k^2 d^{-5}R\Phi, \tag{D 6}$$

and

$$\left(P_V D_I^2 - P_V D_I\right)\Phi + d^{-1}\left[P_V\chi_{-1}D_I\Phi + P_V\chi_{-1}\kappa e^{z_I}M\right]$$
$$+ d^{-2}\left[-P_H k^2\Phi + P_V\chi_{-1}\kappa(e^{z_I} - 1)D_I\Phi + 2P_V\chi_{-1}\kappa e^{z_I}\Phi\right.$$
$$\left. + P_V\kappa\chi_{-1}\left(\kappa e^{2z_I} - \chi_{-1}(z_I e^{z_I} + 2e^{z_I}) + \kappa e^{z_I}(e^{z_I} - 1)\right)M\right] + O(d^{-3}\Phi, d^{-3}M, d^{-2}U)$$
$$= -\eta d e^{z_I}\left[P_5 D_I^2 + P_6 D_I\right]U + \eta\chi_{-1}\left[(z_I e^{z_I} + 2e^{z_I})P_5 D_I^2 + (z_I e^{z_I} + 3e^{z_I})P_6 D_I\right]U$$
$$+ d^{-1}\left[e^{z_I} + \eta\chi_{-1}\frac{K_2 A_2}{K_1}(\kappa e^{z_I}(e^{z_I} - 1) - \chi_{-1}(z_I e^{z_I} + e^{z_I}))D_I^2\right.$$
$$\left. + \eta\chi_{-1}\frac{K_2 A_3}{K_1}(\kappa e^{2z_I} + \kappa e^{z_I}(e^{z_I} - 1) - \chi_{-1}(z_I e^{z_I} + 2e^{z_I}))D_I + \eta k^2 e^{z_I}P_7\right]U. \tag{D 7}$$

The boundary conditions for the inner solution are $U = D_I U = 0 = D_I\Phi - (1 - d^{-1}\chi_{-1})\Phi$ on $z_I = 0$. As in Bees & Hill (1998) for the gyrotaxis-only case, (D 6) indicates that for a non-trivial solution $R \sim d^5 U$, and we require scalings such that the right-hand side of (D 7) does not appear at leading order. Hence, $U \leqslant O(1)$ and $\eta U \leqslant O(d^{-2})$, eliminating the first two leading-order terms on the right-hand side. For a neutral curve, $\sigma = 0$, and so we search for a self-consistent scaling regime where the model is valid. If we scale at third order such that none of the terms on the right-hand side appear, we obtain $P_H k^2 = 0$, which is not useful. If any terms appear before third order, then it is apparent that $R = 0$ or $\eta = 0$, which are again unhelpful. Thus, we need terms at third order and not before. Thus, consider $U \approx d^{-n}$, where

$n = 1, 2, 3, \ldots$., and write

$$U = \sum_{m=n}^{\infty} U_{-m} d^{-m}, \quad \Phi = \sum_{m=0}^{\infty} \Phi_{-m} d^{-m}, \quad M = \sum_{m=0}^{\infty} M_{-m} d^{-m}, \quad (\text{D 8})$$

$$R = d^{5-n} R_{5-n} + d^{5-n-1} R_{5-n-1} + \cdots. \quad (\text{D 9})$$

To first and second orders, (D 6) and (D 7) provide the same as Bees & Hill (1998):

$$\left. \begin{aligned}
&\Phi_0 = e^{z_I}, \quad \Phi_{-1} = -\chi_{-1} z_I\, e^{z_I} + B\, e^{z_I}, \\
&U_{-n} = a_{-n} z_I^3 + b_{-n} z_I^2 + R_{5-n} k^2 \left(z_I + 1 - e^{z_I} \right), \\
&U_{-n-1} = a_{-n-1} z_I^3 + b_{-n-1} z_I^2 + k^2 R_{5-n-1} \left(z_I + 1 - e^{z_I} \right) \\
&\qquad\quad + k^2 R_{5-n} \left(\chi_{-1} \left(z_I e^{z_I} - 4 e^{z_I} \right) - B e^{z_I} + (3\chi_{-1} + B) z_I + 4\chi_{-1} + B \right),
\end{aligned} \right\} \quad (\text{D 10})$$

where B is a constant of integration. Note that since $d(\mathrm{d}M/\mathrm{d}z_I) = \Phi$, then $M_0 = d^{-1}(e^{z_I} - 1)$, which is of higher order than Φ_0. Matching the inner and outer solutions up to second order in the usual way (see Kevorkian & Cole 1981; Bees & Hill 1998) gives $a_{-n} = a_{-n-1} = b_{-n} = 0$,

$$\left. \begin{aligned}
&(A_{-n+1} + B_{-n+1}) \sinh k - k A_{-n+1} \cosh k = 0, \\
&B_{-n+1} \sinh k + B_{-n+1} k \cosh k - k^2 A_{-n+1} \sinh k = k^2 R_{5-n}, \\
&-k^3 \frac{\cosh k}{2} A_{-n+1} - k^2 \frac{\sinh k}{2} A_{-n+1} + k^2 \frac{\sinh k}{2} B_{-n+1} \\
&\quad + k \cosh k B_{-n+1} = b_{-n-1}.
\end{aligned} \right\} \quad (\text{D 11})$$

We proceed by looking in the region of parameter space where $\eta \sim d^{-2}$ and $n = 1$, since this is the region where gyrotactic and overturning instabilities are of the same order (Bees & Hill 1998). The cell conservation equation at third order in (D 7) becomes

$$P_V D_I (D_I - 1) \Phi_{-2} + P_V \chi_{-1} D_I \Phi_{-1} + P_V \chi_{-1} \kappa e^{z_I} M_0 - P_H k^2 \Phi_0 + P_V \chi_{-1} \kappa (e^{z_I} - 1) D_I \Phi_0$$
$$+ 2 P_V \chi_{-1} \kappa e^{z_I} \Phi_0 = e^{z_I} U_{-1} - \eta_{-2} e^{z_I} (P_5 D_I^2 + P_6 D_I) U_{-1}. \quad (\text{D 12})$$

Here, M is of higher order than Φ and so the M term in (D 7) for d^{-1} is used, and for d^{-2} is omitted. To obtain the solvability condition, we integrate from $-\infty$ to 0, which gives

$$R_4 = \frac{2 P_H}{(1 - \eta_{-2}(P_5 - P_6))}, \quad \text{where } P_5 = A_1 + \frac{K_2 A_2}{K_1} \text{ and } P_6 = \frac{K_2 A_3}{K_1} - A_4. \quad (\text{D 13})$$

The asymptotics break down for sufficiently large $\eta_{-2}(P_5 - P_6)$. This expression, at third order, is the same as in the gyrotaxis case in Bees & Hill (1998), since the effects of phototaxis (via χ) have not yet appeared. Solving the constants yields

$$A_0 = \frac{R_4 k^2 \sinh k}{k^2 - \sinh^2 k}, \quad B_0 = \frac{k^3 R_4 (k \cosh k - \sinh k)}{k^2 - \sinh^2 k}, \quad b_{-2} = k B_0. \quad (\text{D 14})$$

To obtain the solvability condition at fourth order, we integrate the cell conservation equation (D 7) at fourth order from $-\infty$ to 0, which gives

$$R_3 = \frac{4 b_{-2}}{k^2} - \frac{2 R_4 \chi_{-1}}{(1 - \eta_{-2}(P_5 - P_6))}. \quad (\text{D 15})$$

Hence, for a deep layer and weak illumination, the Rayleigh number as a function of wavenumber to $O(d^{-1})$ is given by

$$R(k) = \frac{2P_H d^4}{(1 - \eta_{-2}(P_5 - P_6))} \left[1 + d^{-1} \left(\frac{4k(k - \cosh k \sinh k)}{k^2 - \sinh^2 k} - \frac{2\chi_{-1}}{(1 - \eta_{-2}(P_5 - P_6))} \right) \right]. \tag{D 16}$$

This expression is only valid for $k \leqslant O(1)$, and cannot predict the global most unstable wavenumber over all k. For small χ, this predicts the critical wavenumber as zero, since the function is monotonically increasing in k. Similar expressions can be obtained for other scalings (not shown).

D.2. *Asymptotic analysis for model B*

For model B, none of the K_i, J_i, P_i or A_i terms are constants, and the asymptotic analysis involves much expansion. Since the method is, essentially, the same, we do not repeat the analysis here, but merely summarize the results. Full details are provided in a supplementary material available at journals.cambridge.org/flm.

After the equilibrium solution is found, the perturbation equations reveal that the outer solutions for Φ and U are the same as for model A, and given by $\Phi = 0$ and (D 5). For the inner solution, we rescale using $z_I = dz$. For a non-trivial solution, we require $R \sim d^5 U$. As for model A, we consider $U \leqslant O(1)$ and $\eta U \leqslant O(d^{-2})$, and solutions are constructed and matched up to second order in the usual way. If we look in the region of parameter space where $\eta \sim d^{-2}$ and $n = 1$, as for model A, then the solvability condition at third order provides the leading-order Rayleigh number for an expansion as in (D 9) such that R_4 is given by (D 13). Solvability at fourth order gives

$$\begin{aligned}
R_3 = 4b_{-2} &+ \frac{2(P_{(H,0)}(A_K + C_K) + P_{(H,-1)})}{(1 - \eta_{-2}(P_{(5,0)} - P_{(6,0)}))} + \frac{2R_4}{(1 - \eta_{-2}(P_{(5,0)} - P_{(6,0)}))} \left[\frac{N_K}{4} - \frac{5A_K}{4} \right. \\
&- \frac{C_K}{2} + \eta_{-2} \left\{ \left(\frac{5A_K}{4} + \frac{C_K}{2} \right) (P_{(5,0)} - P_{(6,0)}) + \frac{3}{4} A_{(1,0)} N_K + \frac{1}{2} A_{(1,-1)} + \frac{A_{(4,-1)}}{2} \right. \\
&+ \frac{3N_K A_{(4,0)}}{4} + \frac{K_{(2,0)}}{K_{(1,0)}} \left. \left. \left(\frac{1}{2} A_{(2,-1)} + \frac{N_K}{4} A_{(2,0)} - \frac{1}{2} A_{(3,-1)} - \frac{N_K}{4} A_{(3,0)} \right) \right\} \right], \quad \text{(D 17)}
\end{aligned}$$

where $N_k = (K_{(2,0)}/K_{(1,0)})K_{(1/2,-1)}$ is a constant and the long definitions of $A_{(i,j)}$, $P_{(i,j)}$ and all other constants can be found in the supplementary material. (Note that to see the dependence on χ in this expression requires the full definitions.) Thus, the effects of phototaxis appear at fourth order. As for model A, we can also explore other scalings to compare with numerical results (not shown).

REFERENCES

BEES, M. A. & CROZE, O. A. 2010 Dispersion of biased swimming microorganisms in a fluid flowing through a tube. *Proc. R. Soc. Lond.* A, **466** (2119), 2057–2077.

BEES, M. A. & HILL, N. A. 1997 Wavelengths of bioconvection patterns. *J. Exp. Biol.* **200**, 1515–1526.

BEES, M. A. & HILL, N. A. 1998 Linear bioconvection in a suspension of randomly swimming, gyrotactic micro-organisms. *Phys. Fluids* **10**, 1864–1881.

BEES, M. A., HILL, N. A. & PEDLEY, T. J. 1998 Analytical approximations for the orientation distribution of small dipolar particles in steady shear flows. *J. Math. Biol.* **36**, 269–298.

CASH, J. R. & MOORE, D. R. 1980 A high order method for the numerical solution of two-point boundary value problems. *BIT* **20**, 44–52.

CHILDRESS, S., LEVANDOWSKY, M. & SPIEGEL, E. A. 1975 Pattern formation in a suspension of swimming microorganisms: equations and stability theory. *J. Fluid Mech.* **69**, 591–613.

VAN DYKE, M. 1968 *Perturbation Methods in Fluid Mechanics*. Academic.

GHORAI, S. & HILL, N. A. 2005 Penetrative phototactic bioconvection. *Phys. Fluids* **17**, 074101.

GHORAI, S., PANDA, M. K. & HILL, N. A. 2010 Bioconvection in a suspension of isotropically scattering phototactic algae. *Phys. Fluids* **22**, 071901.

HÄDER, D.-P. 1987 Polarotaxis, gravitaxis and vertical phototaxis in the green flagellate *Euglena gracilis*. *Arch. Microbiol.* **147**, 79–83.

HEGEMANN, P. & BRUCK, B. 1989 Light-induced stop response in *Chlamydomonas reinhardtii*: occurrence and adaptation phenomena. *Cell Motil. Cytoskel.* **14**, 501–515.

HILL, N. A. & BEES, M. A. 2002 Taylor dispersion of gyrotactic swimming micro-organisms in a linear flow. *Phys. Fluids* **14**, 2598–2605.

HILL, N. A. & HÄDER, D.-P. 1997 A biased random walk model for the trajectories of swimming micro-organisms. *J. Theor. Biol.* **186**, 503–526.

HILL, N. A., PEDLEY, T. J. & KESSLER, J. O. 1989 Growth of bioconvection patterns in a suspension of gyrotactic micro-organisms in a layer of finite depth. *J. Fluid Mech.* **208**, 509–543.

HINCH, E. J. & LEAL, L. G. 1972 Note on the rheology of a dilute suspension of dipolar spheres with weak Brownian couples. *J. Fluid Mech.* **56**, 803–813.

JONES, M. S., LE BARON, L. & PEDLEY, T. J. 1994 Biflagellate gyrotaxis in a shear flow. *J. Fluid Mech.* **281**, 137–158.

KAMKE, E. 1967 *Differentialgleichungen Losungsmethoden und Losungen*, vol. 1. Akademische Verlagsgesellschaft Geest and Portig K.-G..

KESSLER, J. O. 1985 Co-operative and concentrative phenomena of swimming micro-organisms. *Contemp. Phys.* **26** (2), 147–166.

KESSLER, J. O. 1986 The external dynamics of swimming micro-organisms. *Prog. Phycological Res.* **4**, 258–305.

KESSLER, J. O. 1989 Path and pattern – the mutual dynamics of swimming cells and their environment. *Comments Theor. Biol.* **212**, 85–108.

KEVORKIAN, J. & COLE, J. D. 1981 *Perturbation Methods in Applied Mathematics*. Springer.

LEAL, L. G. & HINCH, E. J. 1972 The rheology of a suspension of nearly spherical particles subject to Brownian rotations. *J. Fluid Mech.* **55** (4), 745–765.

MANELA, A. & FRANKEL, I. 2003 Generalized Taylor dispersion in suspensions of gyrotactic swimming micro-organisms. *J. Fluid Mech.* **490**, 99–127.

MATTHEWS, P. C. 1988 A model for the onset of penetrative convection. *J. Fluid Mech.* **188**, 571–583.

PEDLEY, T. J., HILL, N. A. & KESSLER, J. O. 1988 The growth of bioconvection patterns in a uniform suspension of gyrotactic micro-organisms. *J. Fluid Mech.* **195**, 223–237.

PEDLEY, T. J. & KESSLER, J. O. 1987 The orientation of spheroidal microorganisms swimming in a flow field. *Proc. R. Soc. Lond.* B **231**, 47–70.

PEDLEY, T. J. & KESSLER, J. O. 1990 A new continuum model for suspensions of gyrotactic micro-organisms. *J. Fluid Mech.* **212**, 155–182.

PLATT, J. R. 1961 'Bioconvection patterns' in cultures of free-swimming organisms. *Science* **133**, 1766–1767.

PLESSET, M. S. & WINET, H. 1974 Bioconvection patterns in swimming microorganism cultures as an example of Rayleigh–Taylor instability. *Nature* **248**, 441–443.

RÜFFER, U. & NULTSCH, W. 1991 Flagellar photoresponses of *Chlamydomonas* cells held on micropipettes. II. Change in flagellar beat pattern. *Cell Motil. Cytoskel.* **18** (4), 269–278.

STRAUGHAN, B. 1993 *Mathematical Aspects of Penetrative Convection*. Longman.

VERONIS, G. 1963 Penetrative convection. *J. Astrophys.* **137**, 641–663.

VINCENT, R. V. & HILL, N. A. 1996 Bioconvection in a suspension of phototactic algae. *J. Fluid Mech.* **327**, 343–371.

VLADIMIROV, V. A., WU, M. S. C., PEDLEY, T. J., DENISSENKO, P. V. & ZAKHIDOVA, S. G. 2004 Measurement of cell velocity distributions in populations of motile algae. *J. Exp. Biol.* **207** (7), 1203–1216.

WAGER, H. 1911 On the effect of gravity upon the movements and aggregation of *Euglena viridis, Ehrb.,* and other micro-organisms. *Phil. Trans. R. Soc. Lond.* B **201**, 333–390.

WHITEHEAD, J. A. & CHEN, M. M. 1970 Thermal instability and convection of a thin fluid layer
    bounded by a stably stratified region. *J. Fluid Mech.* **40** (3), 549–576.
WILLIAMS, C. R. & BEES, M. A. 2011 A tale of three taxes: photo-gyro-gravitactic bioconvection.
    J. Exp. Biol. (in press).
ZHANG, L., HAPPE, T. & MELIS, A. 2002 Biochemical and morphological characterization of sulphur-
    deprived and H2-producing *Chlamydomonas reinhardtii* (green alga). *Planta* **214**, 552–561.